$\pi^{\pm}p$, $K^{\pm}p$, pp, and $\bar{p}p$ elastic scattering from 50 to 175 GeV/c*

D. S. Ayres, R. Diebold, and G. J. Maclay
Argonne National Laboratory, Argonne, Illinois 60439

D. Cutts, R. E. Lanou, Jr., L. J. Levinson, and J. T. Massimo
Brown University, Providence, Rhode Island 02912

J. Litt† and R. Meunier‡
CERN, Geneva, Switzerland

M. Sogard,§ B. Gittelman, and E. C. Loh‖
Laboratory of Nuclear Studies, Cornell University, Ithaca, New York 14850

A. E. Brenner, J. E. Elias, and G. Mikenberg
Fermi National Accelerator Laboratory, Batavia, Illinois 60510

L. Guerriero, P. Lavopa, G. Maggi, C. DeMarzo, F. Posa, G. Selvaggi, P. Spinelli, and F. Waldner
Instituto Nazionale di Fisica Nucleare, Sezione di Bari, Italy

D. S. Barton, J. Butler,¶ J. Fines, J. I. Friedman, H. W. Kendall, B. Nelson, L. Rosenson, and R. Verdier
Laboratory for Nuclear Science, Massachusetts Institute of Technology, Cambridge, Massachusetts 02139

B. Gottschalk
Northeastern University, Boston, Massachusetts 02115

R. L. Anderson, D. Gustavson, K. Rich, D. M. Ritson, and G. A. Weitsch**
Stanford Linear Accelerator Center, Stanford, California 94305

(Received 30 September 1976)

The differential cross sections for the elastic scattering of π^+, π^-, K^+, K^-, p, and $\bar{p}$ on protons have been measured in the t interval -0.04 to -0.75 GeV^2 at five momenta: 50, 70, 100, 140, and 175 GeV/c. The t distributions have been parametrized by the quadratic exponential form $d\sigma/dt = A\exp(B|t|+C|t|^2)$ and the energy dependence has been described in terms of a single-pole Regge model. The pp and K^+p diffraction peaks are found to shrink with $\alpha' \sim 0.20$ and ~ 0.15 GeV^{-2}, respectively. The $\bar{p}p$ diffraction peak is antishrinking while $\pi^{\pm}p$ and K^-p are relatively energy-independent. Total elastic cross sections are calculated by integrating the differential cross sections. The rapid decline in σ_{el} observed at low energies has stopped and all six reactions approach relatively constant values of σ_{el}. The ratio of σ_{el}/σ_{tot} approaches a constant value for all six reactions by 100 GeV, consistent with the predictions of the geometric-scaling hypothesis. This ratio is ~ 0.18 for pp and $\bar{p}p$, and ~ 0.12–0.14 for $\pi^{\pm}p$ and $K^{\pm}p$. A crossover is observed between K^+p and K^-p scattering at $|t| \sim 0.19$ GeV^2, and between pp and $\bar{p}p$ at $|t| \sim 0.11$ GeV^2. Inversion of the cross sections into impact-parameter space shows that protons are quite transparent to mesons even in head-on collisions. The probability for a meson to pass through a proton head-on without interaction inelastically is $\sim 20\%$ while it is only $\sim 6\%$ for an incident proton or antiproton. Finally, the results are compared with various quark-model predictions.

I. INTRODUCTION

An experiment has been performed at Fermilab to measure the forward scattering of $\pi^{\pm}$, $K^{\pm}$, and $p^{\pm}$ by protons using a single-arm spectrometer. This experiment required the design, layout, and commissioning of both the medium intensity high-resolution *M6E* beam in the Meson Laboratory area, and the Single Arm Spectrometer Facility.

To test and calibrate the focusing spectrometer and to make an initial physics contribution, the first experiment was designed to measure elastic and inelastic scattering for the six stable hadrons on both hydrogen and deuterium targets. The incident momenta studied were 50, 70, 100, 140, and 175 GeV/c. The range in invariant four-momentum transfer t covered -0.04 to -0.75 GeV^2 and the range in the Feynman x variable spanned $1.0 \geq x \geq 0.70$. A number of short papers[1-3] have been published reporting on aspects of this work and additional papers are in preparation concerning an impact-parameter analysis of the elastic results and inelastic channels in the triple-Regge region and the resonance region. In this paper, a description of the apparatus and experimental procedures (Secs. II and III) and discussions of the

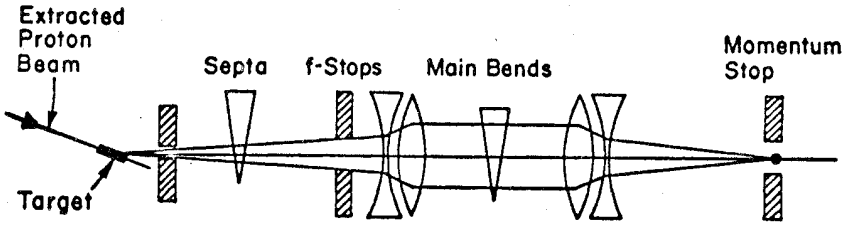

FIG. 1. Diagram of the first stage of the *M6E* beam showing the horizontal plane-optics configuration. The momentum and *f* stops are variable collimators.

data analysis (Sec. IV) and systematic errors (Sec. V) are presented together with the final results for elastic scattering on hydrogen (Sec. VI). In Sec. VII, the results are compared with other measurements of elastic scattering in this energy region. A general discussion of elastic scattering is given (Sec. VIII) in terms of Regge-pole, optical-model, and quark-model concepts.

II. APPARATUS

The experimental technique was (1) to measure the momentum and angle of the incident particle with hodoscopes in the beam and to tag it as a pion, kaon, or nucleon with the beam-line Čerenkov counters, and (2) to measure the momentum and angle of the forward scattered particle and tag it as a pion, kaon, or nucleon using the multiwire proportional chambers and Čerenkov counters of the spectrometer. From this information the total invariant mass squared of all unobserved final-state particles was calculated and used to distinguish elastic from inelastic events. A functional description of the beam and spectrometer systems pertinent to the elastic scattering measurements is given below. A detailed technical description of the facility will be published separately.

A. Beam optics

M6 is one of six secondary beams derived from the Meson Laboratory production target. The beam momentum can be varied from 20 to 200 GeV/c, and the production angle with respect to the extracted proton beam from the accelerator is 2.65 mrad in the laboratory system. The beryllium production target had a square cross section 1.5 mm on the side and was 20.3 cm long.

There are three independent stages of the *M6E* beam with two intermediate foci before the final focus at the experimental target: a collection stage, in which the solid angle and momentum bite are established, a "filtering" stage which suppresses beam halo from the first-stage collimators and production target, and a recombination stage which produces the final achromatic image. Each 150-m-long stage is configured as a point-to-parallel-to-point imaging system with the main bend magnets located in the parallel region to maximize the momentum dispersion. The lens systems are quadrupole doublets configured to maximize the transmission through the 10-cm-wide by 5-cm-high aperture of the bend magnets. A field lens at each intermediate focus serves to maintain the momentum band transmission from stage to stage.

The momentum acceptance is adjustable by means of a collimator up to a maximum of ±0.6%. The angular acceptance can be varied over a range of ±0.56 mrad in horizontal angle and ±0.76 mrad in vertical angle. Figure 1 presents a diagram of the first stage of the beam line and except for the initial septum magnets serves to illustrate the optics of any stage.

Figure 2 shows several ray traces through the beam line to further illustrate the optics. In Fig. 2(a), the two basic rays in the vertical plane are shown, one starting at the origin with maximal divergence and one starting at the extremum object position with zero divergence. Next, in Fig. 2(b), the same two rays are shown in the horizontal plane along with the momentum ray which starts with zero divergence at the origin but with the maximum momentum deviation passed by the beam apertures. Finally, in Fig. 2(c), the beam envelope is shown in both planes using generalized elliptical phase space for the combination of the production target emittance and the beam transmission.

The relative numbers of pions, kaons, and nucleons observed at the hydrogen target are given in Table I. The particle mix is seen to vary strongly as a function of the energy and polarity of the *M6* beam. Yields were typically 10^7 for 2×10^{12} 300-GeV/c protons incident on the Meson Laboratory production target for positive beam and were as low as a few times 10^6 for the negative polarities.

B. Beam instrumentation

The third (recombination) beam stage is fully instrumented to provide trajectory, particle type,

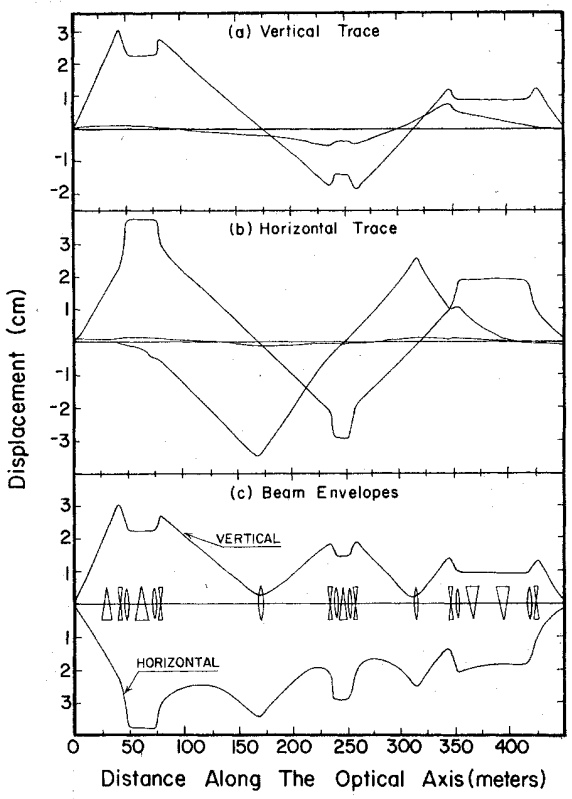

FIG. 2. Ray-trace diagrams for the *M6E* beam line. The vertical trace (a) shows the ray starting at the origin with maximal divergence and the ray starting at the extreme object displacement with zero divergence. In the horizontal trace (b) the same two rays are shown along with a ray starting on the optical axis but with the maximum deviation. The beam-envelope diagrams (c) are computed using elliptical phase space and a schematic representation of the magnetic components for the horizontal plane is included.

and momentum information for each incident particle. Figure 3 shows a layout of the third stage and indicates the position and nature of the detectors. At the second focus, the beam is angle recombined but still highly momentum dispersed. With respect to the production target, the design

TABLE I. Hadron composition of the *M6E* beam flux at the final focus 450*M* from the 8-in. Be production target for 300-GeV/c incident protons.

Particle type	*M6E* momentum (GeV/c) 50	70	100	140	175
π^+	0.760	0.650	0.401	0.210	0.106
K^+	0.025	0.032	0.031	0.026	0.016
p	0.215	0.318	0.568	0.764	0.878
π^-	0.939	0.938	0.938	0.950	0.962
K^-	0.026	0.032	0.041	0.041	0.034
$\bar{p}$	0.035	0.030	0.021	0.009	0.004

parameters at this focus are: vertical magnification = 2.15, horizontal magnification = 1.58, and dispersion = 4.4 cm/% (horizontal). Therefore, with a 1.5-mm production target, the 2.4-mm bin size of the momentum hodoscope at the second focus provides an rms resolution in momentum of ±0.02%.

Downstream of the final beam-line quadrupole magnets, in the drift space before the experimental target, two sets of horizontal and vertical (x-y) hodoscopes located 16.9 m apart determine the incident particle trajectory. The design rms resolution of this system in terms of the beam coordinates at the third focus is ±0.4 mm and ±0.06 mrad in both planes.

Three gas Čerenkov counters, also situated in the third beam stage, were used for particle identification. An extended parallel region provides a suitable location for the operation of the differential counter,[4] which was normally pressurized to respond to nucleons. The DISC counter,[5] which was usually pressurized to respond to kaons, is located at the end of the parallel region, after the recombination dipoles, where the beam is also achromatic. A threshold counter[6] was used to identify pions. At 100 GeV/c, for example, the three counters provided particle identification signals which were >98% efficient with rejections exceeding one part in 10^5.

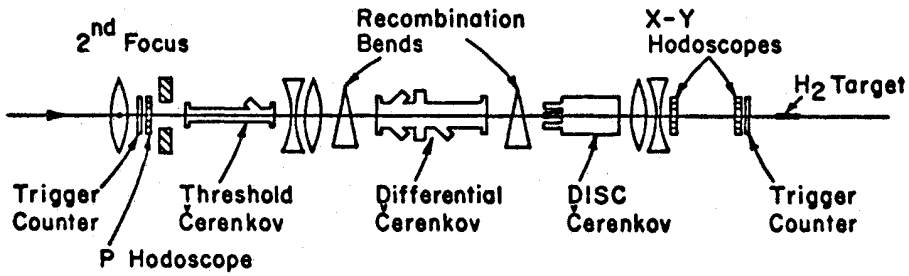

FIG. 3. Diagram of the third stage of the *M6E* beam, including the particle-identification, trajectory, and momentum-tagging instrumentation.

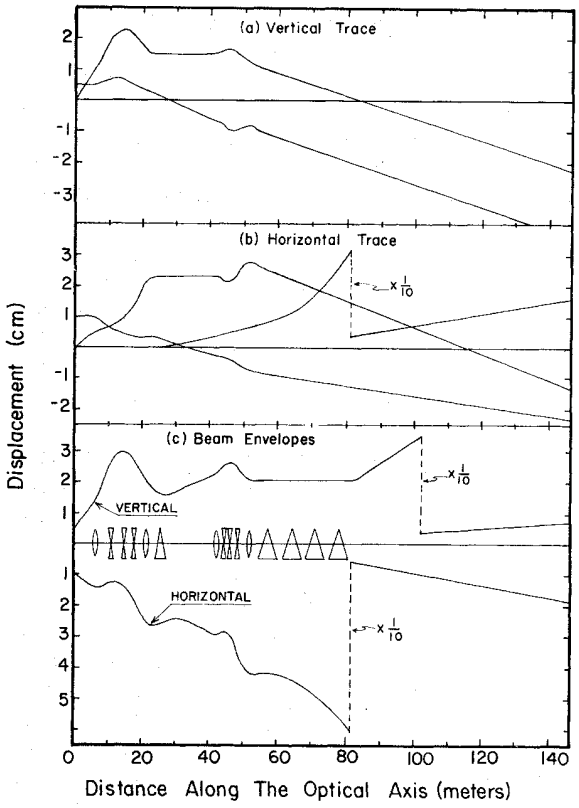

FIG. 4. Ray-trace diagrams for the Single Arm Spectrometer. The vertical trace (a) shows the ray starting at the origin with maximum divergence and the ray starting at the extreme object position with zero divergence. In the horizontal trace (b), the same two rays are shown along with a ray starting on the optical axis but with the maximum momentum deviation. The beam envelope diagrams (c) are computed without phase-space constraints and a schematic representation of the magnetic components for the horizontal plane is included.

C. Spectrometer optics

Since the spectrometer is situated at 0° to the *M6E* beam line and cannot pivot to vary the scattering angle, it can be considered essentially as the fourth stage of the beam line. From this perspective, the spectrometer is a point-to-parallel-to-point beam transport stage using quadrupole-triplet lens systems and instrumented for full determination of particle type, trajectory, and momentum. Five "main-ring" bend magnets disperse the scattered flux in the horizontal plane according to momentum. The total momentum acceptance of the spectrometer is ±3% and the total angular acceptance is 7 μsr. The acceptance was uniform over ±2.5% in momentum and 4.5 μsr in solid angle.

Figure 4 shows several ray traces through the spectrometer analogous to the beam information in Fig. 2. However, the beam envelope is derived from a rectangular initial phase-space distribution instead of the elliptical case appropriate to the beam. At 25 m from the object point (hydrogen target), the vertical magnification ray passes through zero so that the displacement is proportional to the initial divergence (scattering angle) only, with a coefficient of 1 cm per mrad. Further back at 115 m, the horizontal focus has a magnification of 1.8 and a dispersion of 3.7 cm/% so that a 1-mm bin size here along with a 1-mm determination of the incident beam position at the third focus provides a design rms momentum resolution of ±0.03%.

D. Spectrometer instrumentation

Information about the trajectory and momentum of scattered particles is provided by ten multiwire proportional chambers (MWPC's) located at four places along the spectrometer as indicated in Fig. 5. In addition, there is a scintillator hodoscope situated in the focal plane of the front lens system providing redundant information on the vertical-divergence angle. Four remotely adjustable jaw counters at this position can be used to establish the horizontal and vertical angular acceptances of the spectrometer separately.

Three threshold Čerenkov counters[6] and a differential Čerenkov counter[4] serve to identify scattered particles as pions, kaons, or nucleons. The differential counter was normally pressurized to respond to nucleons, and it was equipped with an anticoincidence mirror which gave a signal for pions and kaons with an efficiency which depended on the momentum. For momenta less than 150

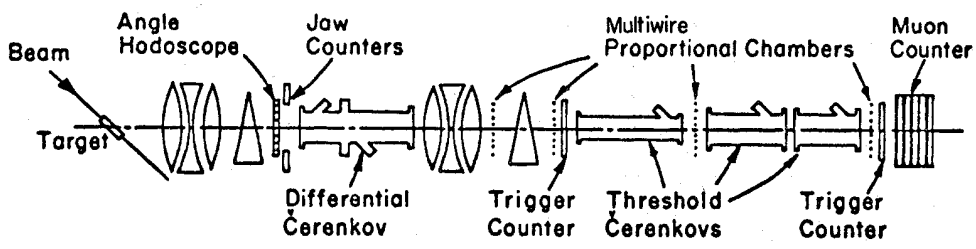

FIG. 5. Diagram of the Single Arm Spectrometer instrumentation and horizontal-plane optics configuration.

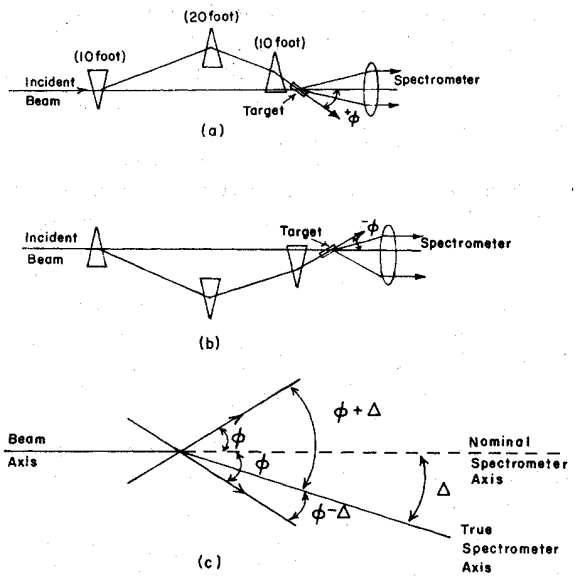

FIG. 6. Variation of the scattering angle by magnetic deflection of the incident beam for the $+\phi$ case in which the beam is deflected down (a) and the $-\phi$ case in which the beam is deflected up (b). A comparison of the results for the two configurations was used to detect a relative angle offset, Δ, as indicated in (c).

GeV/c, the longest threshold counter was set for pions and the two shorter counters were set to respond to both kaons and pions. A kaon event triggered two of the counters while a pion event triggered all three, providing the signature. At higher momenta, where the efficiency of the long threshold counter for pions is significantly less than 100% at kaon threshold, the kaon efficiency of the differential counter antisignal becomes very high, so that all three threshold counters were set for pions to regain the requisite high-detection efficiency. Good rejection ratios (>10^4) were realized for the kaon signal at all energies using these techniques.

The arrays of Čerenkov counters in both the beam line and the spectrometer provided complete tagging of particle type on an event-by-event basis for the incident and outgoing particles separately. In principle, data on nine different reactions could be taken simultaneously. For elastic scattering, data on the three elastic processes were taken simultaneously.

E. Scattering-angle magnet system

The angle between the incident beam and the spectrometer was varied by magnetic deflection of the incident beam. A system of three main-ring bending magnets[7] located just upstream of the hydrogen target was used to pitch the incident beam in the vertical plane as shown in Fig. 6. The magnet spacing is arranged so the beam always crosses the 0° axis at the center of the hydrogen target. Since the incident beam is pitched in the vertical plane and the momentum analysis of the scattered particles is in the horizontal plane, there is no coupling between scattering angle and momentum resolution. The last two magnets are supported by remotely adjustable jack stands, which keep them centered on the beam axis as the angle is varied. The vertical position of the trigger counter and the x-y hodoscope located between the last two pitching magnets is also remotely adjustable, while the liquid hydrogen target simply pivots about its center to track beam-angle variations.

Each of the three magnets in the system was measured with a long flip coil and with an NMR probe so that the magnetic lengths and excitation curves are known to an accuracy of ±0.1%. The pitching magnets are connected in series along with a 3-ft-long monitor magnet of similar construction. Stability and repeatability of the angle settings were continuously monitored with magnetic-field probes located in this monitor magnet. Similar 3-ft magnets were placed in series with the main bend chains in the beam and the spectrometer to monitor the momentum settings. Scattering measurements at an angle ϕ were made symmetrically using the pitching magnets to deflect the beam both up ($-\phi$) and down ($+\phi$) in order to eliminate the systematic effect of any small offset between the beam and the spectrometer (see Fig. 6). Therefore, the t scale is determined only by the fields in the pitching magnets and is independent of the alignment of the beam relative to the spectrometer.

For a scattering event, the angle change is determined by combining the pitching angle of the beam with the incident and outgoing divergence angles as measured by the beam-line hodoscopes and the spectrometer wire chambers. Neglecting the small divergence angles, $-t$ is proportional to the square of the integrated field strength of the pitching magnets times the ratio of the outgoing to the incident momentum for elastic kinematics. The estimated total uncertainty in the magnetic lengths of 0.25% thus leads to a fixed fractional systematic uncertainty in t of 0.5%.

F. Calibrations

The fact that the incident beam can be directed down the spectrometer at 0° greatly facilitated calibration of the spectrometer. By varying the appropriate beam or spectrometer parameters, the optical properties were measured directly. For example, the momentum dispersion coeffi-

TABLE II. Missing-mass and momentum-transfer resolution of the Single Arm Spectrometer–*M6E* beam-line installation for elastic scattering at a momentum transfer squared of 0.1 GeV^2.

Incident momentum (GeV/c)	$\sigma(t)$ (GeV^2)	$\sigma(M_X^2)$ (GeV^2)
50	0.0048	0.131
70	0.0056	0.133
100	0.0069	0.139
140	0.0091	0.150
175	0.0112	0.162

cient at the spectrometer focus was determined by varying the current in the spectrometer magnets with a small 0.05% momentum spread in the incident beam. Absolute momentum calibration of ±0.1% was provided by the index-of-refraction change between pion and proton Čerenkov light at a fixed angle in the DISC counter. A laser interferometer in the counter provided a continuous determination of the index of refraction as the pressure was changed. The total momentum resolution was given directly by the difference between the beam and spectrometer momentum measurement at 0°. The total angular resolution was measured at the same time. The resolutions of the *M6E*-spectrometer system in t and missing mass squared are shown in Table II. The resolution actually realized is poorer than the design resolution because of the effect of multiple scattering, power-supply ripple, and magnetic field irregularities.

Measurements of the solid angle could also be made directly by using the scattering-angle pitching magnet system. For the vertical-angle hodoscope in the focal plane of the front lens system, varying the incident angle at the hydrogen target causes the beam image to move across the counters, giving a direct measurement of the angle dispersion there. In actual practice, the transmission through the jaw counters at the same location proved a more efficient diagnostic. If the final beam-line lens system is turned off, the beam incident to the spectrometer is parallel and is brought to a sharp focus on the plane of the jaw counters. Varying the incident angle with the pitching magnets causes the image to sweep across the jaw counters; the full width at half maximum (FWHM) of such a transmission curve in terms of incident angle gave a direct determination of the angular dispersion. An example of this procedure is given in Fig. 7.

By operating the spectrometer at 0° at the same momentum as the beam, it was possible to measure the performance of the Čerenkov counters, without the need to repeat the pressure curves. By making use of the particle-identification redundancy present when the two sets of counters, beam and spectrometer, were illuminated with the same particle flux, the efficiency and rejection ratio for each counter were determined. Such 0° calibration runs were frequently taken during the course of the elastic measurements, not only to check the Čerenkov-counter performance, but to monitor the spectrometer optics and efficiency and to verify the system momentum resolution. A model of the spectrometer was set up using the measured properties of the magnets and then codified according to the beam-optics computer program TRANSPORT.[8] Since the direct measurements of various optics coefficients agreed with the values from this model to better than 2%, all cross-section results have been obtained using parameters of the model. All calculations were carried out to second order. The horizontal and vertical planes were not coupled except through momentum. The ray-trace and beam-envelope graphs shown in Figs. 2 and 4 are first-order calculations based on TRANSPORT models for the optics.

G. The on-line system

A PDP11/45 computer with the SPEX multitasking system[9] was used for the data collection. The associated hardware included storage-type cathode-ray-tube (CRT) display, two disk memories, magnetic tape, and DEC tape units, an electrostatic

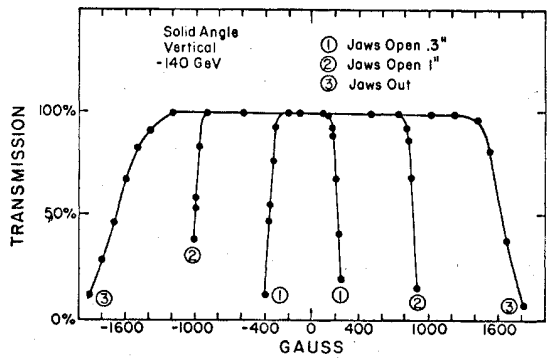

FIG. 7. Curves of the 0° spectrometer transmission through the aperture-defining jaw counters for three settings of the jaws as a function of the incident beam angle measured in field strength of the scattering angle magnet system. The ratio of the FWHM for curves 1 and 2, 0.306, compared with the ratio of the jaw openings, 0.305, is a check on the measurement. Curve 3 shows the physical aperture of the spectrometer as defined by magnet steel when the jaws are fully open.

printer/plotter, and 28 000 words of core memory. SPEX loaded the programs from the disk in response to internal and external conditions. Several "tasks" could be run at once with SPEX handling their communication and synchronization.

The on-line system was used to record events and running conditions, perform a simple data analysis including a cross-section calculation, and monitor the equipment. It also aided in setting high voltages and timing delays for the hodoscopes and MWPC's, checking beam optics and steering, and doing other setup and checkout chores. Conditions set up at the beginning of each run included the target (hydrogen, deuterium, or empty) and central values for the spectrometer angle, spectrometer momentum, and beam momentum. At the start of each run the magnetic field strength in the beam, spectrometer, and angle-varying bend magnets, the Čerenkov pressures and temperatures, and the position of most movables such as the target, some counters, and the pitching magnets, were read into the computer. These and the on-line system parameters were printed and written on magnetic tape. Following a system reset of the electronics, the computer was switched to the event acquisition mode. An event consisted of 50 to 70 16-bit words read via CAMAC and the wire-chamber interface. Typical runs included 5000 to 65 000 events. Tape speed and buffer size limited the data taking to about 200 events or 14 000 words per accelerator spill.

The computer decoded both beam and spectrometer event data (see Sec. III) and created tables of hodoscope and MWPC efficiencies, counts of events passing various cuts, counts of particle and reaction types, beam profiles at each detector, pulse-height spectra, and other diagnostic aids. Simultaneously, the events, exactly as read, were written to a magnetic tape for the off-line analysis. For selected spectrometer events, particle trajectories were reconstructed using first- and second-order TRANSPORT matrices. Events were then binned by scattering angle and momentum loss for the cross-section calculation done at the end of the run. Various phase-space projection histograms were also created. It was possible to display any histogram on a CRT or make a permanent copy at any time during the run. At the end of a run the diagnostic and summary tables with the final scalar readings, various counting-rate ratios of interest, beam-spot size and focus location, the kinematic running conditions, and plots of all the histograms were printed out. During the run a scanning digital voltmeter was used periodically to read the counter high voltages, and the on-line system compared these readings to a table of standards, signaling any errors.

H. Target system

Six targets were available for this experiment: 25-cm and 50-cm-long liquid-hydrogen targets, 25-cm and 50-cm liquid-deuterium targets, and 25-cm and 50-cm dummy (evacuated) cells. All targets were 1-in. diameter Mylar tubes with hemispherical Mylar endcaps. The wall thickness was 5 mils, and the endcap thickness was 3 mils. All six cells were housed in a single aluminum scattering chamber which was under vacuum, with 7.5-mil Mylar entrance and exit windows. Superinsulation was wrapped around each cell. The liquid hydrogen was produced and maintained by a closed-loop refrigeration system which used cold helium gas as the refrigerant. In normal operation, the liquid hydrogen was at atmospheric pressure. A vapor-pressure gauge monitored the target density. During the experiment, target operation was stable and no boiling or icing was observed. The pipes between the hydrogen reservoir and the target cell were inclined at 5° to the horizontal so that the cells would stay full as they were tilted to track the scattering angle.

The target assembly could be moved remotely to position the desired target on the beam line. Target scans verified the alignment of the cells with the beam. Since the cells were much larger than the beam spot, the alignment was not critical.

I. Recoil particle detection

Two hodoscopes[10] located below the target were used to measure the z coordinate (position along the target length) and azimuthal angle of the recoiling proton. These hodoscopes only intercepted the recoil proton from elastic scatters when the incident beam was pitched down. Their use in the elastic experiment on hydrogen is discussed in Sec. IV. The hodoscopes play a central role in the analysis of data taken on the deuterium target.

III. RUN PLAN AND DATA TAKING

The spectrometer vertical angular acceptance of ±1.5 mrad necessitated several incident angle settings to cover the t interval from −0.04 to −0.75 GeV^2. The spectrometer momentum acceptance of ±2.5% contained the elastic peak and the inelastic spectrum out past the resonance region. Only the excitation of the angle pitching magnets had to be altered to vary the scattering angle, with the spectrometer-magnet currents and Čerenkov-counter pressures being held constant.

Central angle settings of 3.5 to 17.0 mrad were required to cover the t interval of interest at 50 GeV/c. At 175 GeV/c, settings of 2.5 to 4.0 mrad were required. Central settings were spaced by

1.5 mrad—one half of the spectrometer acceptance—to provide a consistency check in adjacent runs. Čerenkov-counter deployment varied slightly with incident energy to exploit the strengths of the various counters.

The basic data-acquisition cycle was:

(1) Empty target: $+\phi$,
(2) Full target: $+\phi$,
(3) Full target: $-\phi$,
(4) Empty target: $-\phi$.

Data taking was influenced by the total flux and composition (particle mix) of the beam at each energy. When $\sim 2\times10^{12}$ 300-GeV/c protons were incident on the meson production target, several million secondaries scattered into the $M6$ beam. A rate of approximately 2.2×10^{6} particles/pulse was found to be optimal from the point of view of pileup effects, and typically the collimators were adjusted to reduce the flux to this level. At low-t values, where the event rate was so high that data acquisition was computer-dead-time limited, electronic suppression (countdown) circuits were used in the beam trigger to reduce the number of triggers on abundant particles (π^+, p, or π^-) so as to enrich the number of minority particle ($K^+, K^-, \bar{p}$) initiated events.

At 140 and 175 GeV/c, it was necessary to go to very small angles (1.5 to 2.5 mrad) to achieve low-t values. Special procedures were necessary to reduce backgrounds from the unscattered beam which was then just at the edge of the spectrometer acceptance. Most of the beam was vetoed by four scintillation "jaw" counters which were positioned to form a precise rectangular acceptance at the spectrometer angle focus. Finally, to protect the wire chambers from the high rates of the unscattered beam, a steel scraper block was placed downstream of the jaw counters. The relative placement of the scraper and the jaw counters, shown in Fig. 8, was such that the aperture

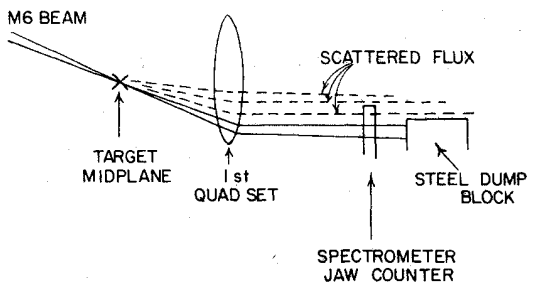

FIG. 8. Setup for small-angle scattering. The unscattered beam (solid line) passes through the jaw counter and into the iron dump block. The acceptance for scattered flux is determined by the edge of the scintillator jaw counter.

was always defined by scintillator and never by steel.

In addition to triggering on scattered events ("spectrometer events"), the system was also triggered on a sample of the incident-particle flux unbiased by the requirement of scattering into the spectrometer. This sample of "beam events" was used to compute corrections to the scaled incident flux for the effect of any selection requirements which were applied to the incident particle of a scattering event. It also allowed a determination of beam hodoscope and Čerenkov efficiencies, and a measurement of the position, size, and angular divergence of the beam.

IV. DATA ANALYSIS

A. Multiple analyses

Many preliminary studies, both on-line and off-line, were necessary to understand fully the properties of the apparatus. From these studies the best algorithms for geometric reconstruction of the events and for particle identification were chosen. Finally, three different and independent cross-section calculations were undertaken by three different subgroups of the collaboration. The main differences among the calculations related to the criteria for selecting events for inclusion in the cross sections and to the details of the acceptance calculations. The comparison of the results provided a valuable measure of the possible biases and errors associated with the various cuts and selection criteria. The averaging procedure by which the results were combined is discussed below.

B. Event reconstruction

The three beam-line Čerenkov counters were used to classify the incident particle as a pion, kaon, or nucleon. The four spectrometer Čerenkov counters were used to classify the scattered particle type. The momentum angles, and position of the incident particle at the hydrogen target were calculated from the beam-line hodoscope data. The trajectory of the scattered particle at the back of the spectrometer was determined from the MWPC information. This trajectory was traced backward through the magnets of the spectrometer, using the known transfer matrix to obtain the momentum, angles, and position of the scattered particle at the hydrogen target. The measurement of the scattered momentum was improved by constraining the scattered trajectory to agree with the horizontal coordinate of the incident particle at the hydrogen target.

A good track in an MWPC was defined as a single cluster of adjacent struck wires (no missing wires

within the cluster) with fewer than some maximum number of wires (typically ~3). Individual chamber efficiencies ranged from (95 to 98)%. Although only 75% of all events had good tracks in *all* 10 MWPC's, it was *not* necessary for every chamber to have a good track in order to completely reconstruct the trajectory. Extensive studies were carried out to determine the configurations of chambers with good tracks which allow complete reconstruction without degrading the overall momentum or angular resolution. The resulting reconstruction efficiency was ~97% and was uniform over the aperture of the spectrometer.

A good track in a beam hodoscope was defined as a single hit or two adjacent hits. Although, strictly speaking, a good track in each of the five hodoscopes was necessary to completely determine the incident particle trajectory, only the momentum hodoscope and the target x hodoscope were absolutely essential to the measurement of the missing mass with high resolution. The other three hodoscopes were involved in angle measurements and provide very small corrections to the t scale. These corrections could be included on an event-by-event basis or in an average way for the whole run. The event-by-event approach was used in two analyses and the average-correction approach, which accepted about 20% more events, was used in the third.

Because of the rf structure of the beam, roughly 10% of the time two particles came down the $M6$ beam line essentially simultaneously and produced two tracks in the beam hodoscopes. All such events were considered to fail beam reconstruction and the calculated cross sections were corrected accordingly.

C. Calculation of uncorrected cross sections

From the coordinates of the incident and scattered particles, the missing mass squared and scattering angle were calculated for each event. Events were then subjected to various selection requirements and entered into histograms which formed the basis of the cross-section calculation. The selection criteria were as follows:

(i) Successful reconstruction of the incident and scattered trajectory.

(ii) Identification of the event as an elastic scatter. The incident particle had to be unambiguously identified as a pion, kaon, or nucleon; the missing mass squared had to satisfy a cut for elastic scattering. Once an event had satisfied this missing-mass cut, the identity of the incident particle alone was sufficient to classify the type of elastic scattering (π, K, p) because other processes which could produce a signal in the elastic peak are heavily suppressed by dynamics. The identification of the scattered particle provided by the spectrometer Čerenkov counters was available as a redundant check on the elastic nature of the events.

(iii) Satisfaction of geometric-acceptance cuts. Geometric-acceptance cuts were placed on the horizontal and vertical scattering angles. For π^+, π^-, and p, these cuts restricted the events to the uniform-acceptance region of the spectrometer. More generous cuts were applied to K^+, K^-, and $\bar{p}$, and the acceptance was calculated by a procedure described below.

For a given reaction the yield $Y(\phi_i, \Delta\Omega)$ into the ith histogram bin of solid angle $\Delta\Omega$ centered on angle ϕ_i was related to the cross section $d\sigma/d\Omega(\phi_i)$ at the center of the bin as

$$Y_i(\phi_i, \Delta\Omega) = \rho N_A l B \epsilon_B C_{\text{abs}} \epsilon_S \epsilon_C \epsilon_{\text{acc}} C_{\text{res}} \Delta\Omega \frac{d\sigma}{d\Omega}(\phi_i), \tag{1}$$

where

ρ = density of liquid hydrogen target at atmospheric pressure,

l = length of hydrogen target,

N_A = Avogardro's number,

B = total flux for this incident particle type,

ϵ_B = fraction of flux surviving incident-particle selection requirements, determined from the beam-event sample,

C_{abs} = spectrometer "transmission" for this particle type. This was reduced from 1 owing to absorption of the incident and scattered flux by the material of the target, absorption of scattered flux by the material of the spectrometer, and decays.

ϵ_S = spectrometer reconstruction efficiency,

ϵ_C = spectrometer Čerenkov efficiency for identifying this particle type,

ϵ_{acc} = average acceptance correction (defined below),

C_{res} = corrections for bin-size and angular-resolution effects and for the finite size and divergence of the incident beam,

$\Delta\Omega$ = total nominal solid angle of bin.

The cross section was converted to its invariant form $d\sigma/dt$ at the point $-t = (p_{\text{inc}}\phi)^2/(1 + p_{\text{inc}}\phi^2/2M_p)$ by multiplying $d\sigma/d\Omega$ by the Jacobian $\pi/[p_{\text{inc}}(p_{\text{inc}} - |t|/2M_p)]$ (M_p is the proton rest mass).

The correction factor C_{res} was of the order of 10% and was accurate to at least 5% of its value. Its calculation is described elsewhere.[11] For abundant particles, π^+, π^-, and p, only events falling within the uniform-acceptance region of the spectrometer were accepted, so that $\epsilon_{\text{acc}} = 1.0$. For minority particles, K^+, K^-, and $\bar{p}$, an extended acceptance region was used. The average acceptance for minority particles was determined by comparing the ratio of a majority particle (π^+ or π^-) yield, Y_u, within the uniform-acceptance re-

gion to the yield Y_{ext} for the same particle in the extended acceptance region:

$$\epsilon_{acc} = \frac{Y_u}{Y_{ext}} = \frac{\Delta\Omega(\text{uniform})}{\Delta\Omega(\text{extended})} . \quad (2)$$

In this manner, pions were used to measure the edges of the acceptance.

D. Run combination

The empty-target and full-target cross sections were calculated separately and then subtracted. The $+\phi$ and $-\phi$ runs nearly always had comparable statistical accuracy and were averaged with equal weights to remove the effects of small angle offsets between the beam and spectrometer to first order. More sophisticated averaging procedures which eliminated higher-order effects of offsets did not significantly change the results.

E. Combination of results from different analyses

Detailed comparisons of the results of the three different analyses showed them to be reasonably consistent. The typical level of agreement was 1% on slope parameters and 2% on absolute normalization. The results were averaged together with equal weights. Care was taken to include in the error calculation the fact that the results were drawn from the same data and did not represent independent measurements.

F. Final corrections to cross sections

Several corrections had to be applied to the raw yields and fluxes to convert them to absolutely normalized hadronic cross sections. The data for these corrections were measured on-line by taking special runs. The measurements were greatly facilitated by the fact that with the angle-pitching magnets turned off, the beam passed directly into the spectrometer. The beam could be swept across the spectrometer in the vertical plane by varying the pitching-magnet excitation, and its position at the entrance of the spectrometer could be varied using the beam-line vernier magnets.

1. Detector efficiencies

a. Spectrometer reconstruction efficiency. The tracking algorithms successfully reconstructed $(97 \pm 1)\%$ of the scattered events. The efficiency was constant over the uniform acceptance part of the aperture.

b. Particle identification. The complete tagging of both the incident and scattered particle type with a total of seven Čerenkov counters reduced to a negligible level errors in the elastic yields owing to misidentification of particles. The efficiency of particle identification for the scattered particle was always greater than 97% and was known to a few tenths of a percent from 0° runs.

Particle misidentification was measured by comparing the beam and spectrometer identifications on 0° runs, and was negligible except at 100 GeV/c. For the 100-GeV/c running, the beam differential Čerenkov counter had not yet been installed. The beam identification for protons was by default—all beam particles not labeled as pions or kaons were considered protons. Under these circumstances, ~0.5% of the pions were labeled as protons. Again, the proton identification in the spectrometer was sufficiently powerful to eliminate mislabeling of scattered events, and the only problem was associated with counting the incident flux. For the worst case, the error in the $\bar{p}$ flux at 100 GeV/c was ~15%. Data from frequent 0° runs were used to correct p or $\bar{p}$ fluxes, resulting in final errors in the flux of less than 1%.

2. Dead time, accidentals, and rate corrections

A fast gating system ensured that all the electronics, including the flux scalars, were gated synchronously to avoid any dead-time corrections. The rates in the spectrometer were always low (<20 000 events/pulse) compared to the capabilities of the detectors. The primary accidental effects were associated with the counting of the beam flux.

The rf structure of the beam eliminated conventional dead-time losses, leaving pileup effects as the only rate-dependent problem. The time resolution of the trigger counters was insufficient to resolve individual particles within a single rf bucket and this produced an error in counting the incident particle flux. Although the particles within a bucket could not be separated in time, they could be detected by the appearance of two tracks in the beam-line hodoscopes. The efficiency for detecting two particles in a bucket was ~97%. At rates of 1.5 to 2.6×10^6 particles/pulse, typically 10% of the rf buckets contained more than one particle. The residual error in counting the beam flux was less than 0.3%.

Checks were made for additional rate and dead-time effects by taking a series of runs at rates of 1, 2, and 3×10^6 particles/pulse. Cross sections calculated from these runs were consistent at the 1% level of statistical accuracy.

3. Absorption and decay corrections

Yields were reduced by absorption of the incident flux in the material of the final beam trigger counter and the hydrogen target, and of the scattered flux in the target and in the material of the spectrometer. For pions and kaons, there was also a

loss of events due to decays. The survival rate between the final beam trigger counter and the end of the spectrometer for each particle type was measured directly by passing the beam into the spectrometer in 0° runs. These runs were taken with the hydrogen target cell in place, with the dummy target cell in place, and with no cell at all in the beam. The transmission numbers obtained were consistent with calculations based on the material present, using the known absorption cross sections,[12] and the lifetimes of the particles. The spectrometer transmission without the target in place was typically (90–95)% and varied with the particle type and the momentum.

4. *Contamination of incident pion flux by leptons*

Incident pions were tagged with a threshold counter which was also sensitive to electrons (positrons) and muons. The muon flux near the target was determined in special runs by measuring the transmission of tagged "pions" through 10 ft of steel. The electron flux was measured with a shower counter during 0° runs. Typically, the beam contained (1 ± 0.25)% muons and (1 ± 0.25)% electrons.

5. *Contamination of elastic yields by inelastic events*

The missing-mass-squared (MM^2) resolutions are given in Table II. These should be compared with the gap of 0.28 GeV^2 in MM^2 between the elastic peak and inelastic threshold. The prominent diffractively produced resonances near 1650 MeV/c^2 and the nondiffractively produced $\Delta(1236)$ are separated by several standard deviations from the elastic peak and therefore do not contaminate the elastic signal. Only final states produced very near inelastic threshold have any possibility of producing background under the elastic peak.

Several approaches were used to determine the inelastic contamination:

(1) The resolution function of the apparatus in MM^2 was determined from 0° runs. This resolution function was normalized to the low-missing-mass side of the peak from a large-statistics scattered run. A small excess on the high-missing-mass side was observed and was interpreted as inelastic background (see Fig. 9). This procedure was carried out at several angles to extract the t dependence.

(2) An attempt was made to extrapolate the observed low-mass inelastic spectrum down below the elastic peak. This procedure was satisfactory because the background was negligible at 50 GeV/c owing to the relatively good missing-mass-squared resolution. The 175-GeV/c resolution function was folded into the 50-GeV/c inelastic spectrum to see what additional contamination was introduced by the poorer MM^2 resolution at the higher energy.

(3) For part of the running, a hodoscope which measured the azimuthal angle of the recoiling proton was located beneath the target. The additional requirement of coplanarity between the fast (spectrometer) particle and the recoiling proton eliminated most of the remaining inelastic events in the vicinity of the elastic peak.

All three procedures indicated an inelastic contamination of less than 1% at low t ($t \sim -0.1$ GeV^2) and a (3–4)% contamination at $t \sim -0.7$ GeV^2. The percent contamination did not seem to be a strong function of particle type.

6. *Corrections for electromagnetic effects*

Corrections were made for Coulomb scattering and radiative effects.

a. Coulomb scattering. The low-t points were just at the edge of the Coulomb interference region. The correction was calculated from the formula due to Bethe,[13] with the phase of the Coulomb amplitude as calculated by West and Yennie.[14] The dipole form factor

$$G(t) = \frac{1}{(1 + |t|/0.71\ \mathrm{GeV}^2)^2} \tag{3}$$

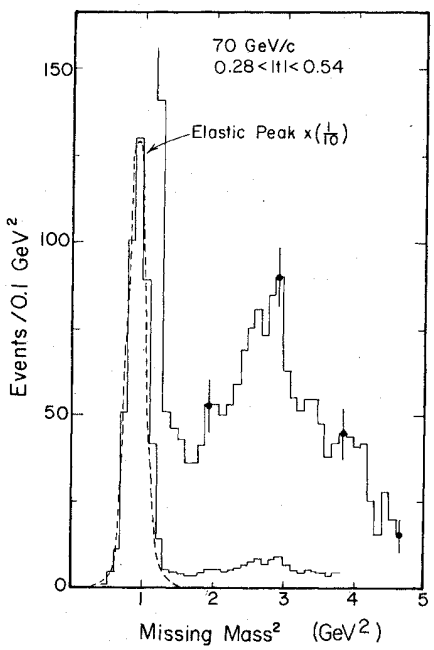

FIG. 9. Missing-mass-squared spectrum at +70 GeV/c for elastic and near-elastic pion-proton scattering in the t range indicated. A Gaussian distribution has been drawn through the elastic yield to indicate the amount of inelastic background under the elastic peak.

TABLE III. Typical contributions of t-dependent corrections to differential cross sections: $(d\sigma/dt) = (d\sigma/dt)|_{\text{raw}} C_r C_c C_D C_I$.

p (GeV/c)	Particle	$-t$ (GeV^2)	Radiative correction C_r	Coulomb correction C_c	Double-scattering correction C_D	Inelastic background C_I
70	π^+	0.025	1.01	0.98	1.00	0.99
		0.400	1.05	1.00	0.99	0.98
		0.660	1.07	1.00	0.98	0.96
	p	0.026	1.00	0.98	1.00	0.99
		0.400	1.00	1.00	0.98	0.98
		0.630	1.00	1.00	0.94	0.96
	K^+	0.030	1.00	0.99	1.00	0.99
		0.400	1.01	1.00	1.00	0.98
		0.650	1.02	1.00	0.99	0.96
175	π^+	0.060	1.02	1.00	1.00	0.99
		0.370	1.06	1.00	0.99	0.98
		0.730	1.08	1.00	0.98	0.94
	p	0.060	1.00	1.00	1.00	0.99
		0.370	1.00	1.00	0.98	0.98
		0.730	1.00	1.00	0.92	0.94
	K^+	0.060	1.00	1.00	1.00	0.99
		0.370	1.01	1.00	1.00	0.98
		0.670	1.02	1.00	0.99	0.95

was used to describe the charge distributions for all particles. The three pieces of information required for the computation are the total cross sections, the ratio of the real to imaginary parts of the forward elastic amplitudes, and the elastic slope. The total cross sections were taken from the measurements of Carroll *et al.*[15]; the real-to-imaginary-part ratios were taken from Refs. 18 to 20, and the forward slopes from the uncorrected results of this experiment. These corrections were never more than 3% so that errors of ~10% in any of the input quantities are insignificant.

b. Radiative corrections. The calculation for loss of events from the elastic peak due to radiation of photons has been performed by Sogard.[16] In this experiment, the correction is significant only for pions: It increases from zero at $t = 0$ to ~7% at $t = -0.8$ GeV^2 for the missing-mass-squared cuts used in the analysis.

7. *Double-scattering corrections*

A particle which has scattered once may scatter a second time before it leaves the hydrogen target. The angular distribution of double scatters is different from the distribution of single scatters. In particular, two small-angle scatters may stimulate a large-angle scatter, thereby artifically increasing the cross section at large t. Corrections for this effect were made by analytic calculation and by Monte Carlo simulation. The effect is appreciable for reactions with very steep forward slopes, such as proton and antiproton scattering and was ~10% for protons at $t \sim -0.7$ GeV^2.

Table III shows the size of the Coulomb, radiative, double-scattering, and inelastic background corrections at two selected energies—70 and 175 GeV/c—and at three t values.

V. DISCUSSION OF SYSTEMATIC UNCERTAINTIES

Systematic uncertainties in the absolute normalization were mainly due to imprecise knowledge of the spectrometer solid angle (±2%) and uncertainties in the spectrometer transmission and reconstruction efficiency (±1%). Uncertainties in the electron and muon contamination, the absolute momentum calibration, the horizontal-angle alignment of the beam and spectrometer, and accidental corrections contributed all together less than 1%. An overall normalization uncertainty of ±3% has been assigned to the results to account for these effects.

Systematic errors in the t scale arose from uncertainties in the magnetic length of the angle pitching magnet system and residual misalignments of the beam and spectrometer axes. An overall uncertainty of ~1.5% was assigned to the t scale. The implications of this 1.5% uncertainty are as follows:

(i) Linear slope parameters of the differential cross sections have a 1.5% systematic uncertainty.

(ii) Individual cross-section points have fractional errors of $B(t)\Delta t$, where Δt is the absolute un-

certainty in t and $B(t)$ is the local logarithmic derivative. At $-t = 0.7$ GeV^2 for $B(-0.7) \sim 6$ to 8 GeV^{-2}, the error is (6 to 8)%.

Point-to-point systematic errors were negligible due to the excellent uniformity of the geometric-reconstruction efficiency. Measurements of the same t values in different parts of the aperture generally agreed within statistical accuracy.

An error in setting the field of the angle pitching magnets could shift the t scale and cause errors in the cross section. Adjacent kinematic settings overlapped by ~1.5 mrad ($\frac{1}{2}$) the spectrometer acceptance), providing a very sensitive check against such errors.

Systematic errors arising from uncertainties in the corrections to the data discussed above are less than 2% even at large-t values.

VI. RESULTS

The results consist of angular distributions for π^+, π^-, K^+, K^-, p, and $\bar{p}$ elastic scattering on protons at 5 momenta: 50, 70, 100, 140, and 175 GeV/c. Fully corrected data points for the 30 angular distributions are listed in Table IV and are displayed in Fig. 10. Only statistical uncertainties are given. In order to produce tabulations of reasonable size, the cross sections have been binned on a t grid which is coarser than the t resolution of the apparatus. (Detailed studies of the cross

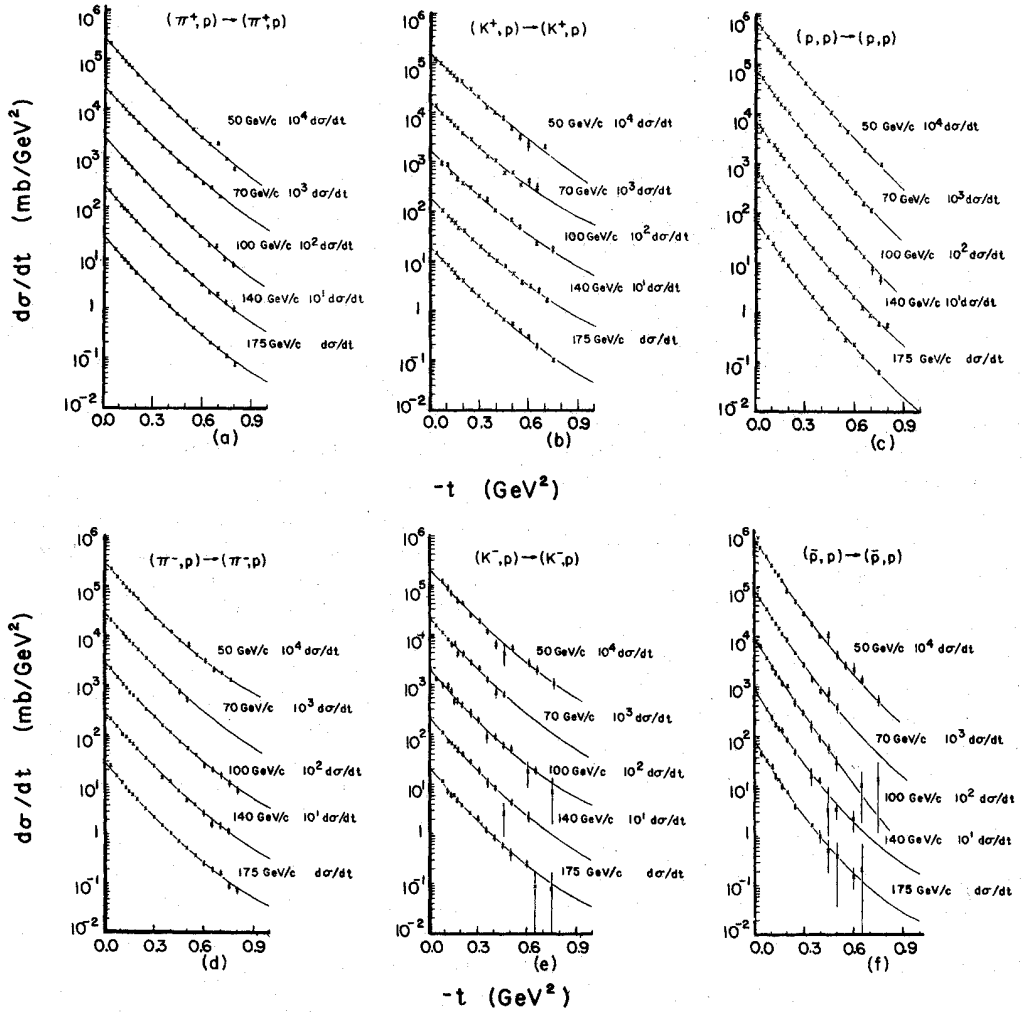

FIG. 10. Plots of fully corrected cross sections. (a)–(f) show π^+p, K^+p, pp, π^-p, K^-p, and $\bar{p}p$, respectively, at all five momenta. In order to provide separation between the results for 50, 70, 100, 140, and 175 GeV/c, the cross sections have been scaled by 10 000, 1000, 100, 10, and 1, respectively. Only statistical errors are plotted. The smooth curves are plots of the parametrizations of Table V. The point at $t = 0$ is the optical-theorem prediction given in Table V.

TABLE IV. Tabulation of differential cross sections. Only statistical uncertainties are included.

a. 50 GeV/c

$\pi^+p\to\pi^+p$		$K^+p\to K^+p$		$pp\to pp$	
$-t$ (GeV^2)	$d\sigma/dt$ (mb/GeV^2)	$-t$ (GeV^2)	$d\sigma/dt$ (mb/GeV^2)	$-t$ (GeV^2)	$d\sigma/dt$ (mb/GeV^2)
0.0375	20.71±0.52	0.0375	11.84±0.59	0.0375	51.48±0.74
0.075	14.27±0.19	0.075	9.70±0.39	0.075	35.54±0.32
0.110	10.43±0.25	0.110	7.45±0.47	0.110	25.03±0.46
0.130	9.00±0.19	0.130	6.10±0.56	0.130	20.26±0.44
0.150	7.66±0.24	0.150	5.38±0.45	0.150	16.69±0.36
0.170	6.67±0.25	0.170	4.63±0.44	0.170	13.61±0.45
0.200	5.00±0.13	0.200	4.35±0.34	0.200	10.50±0.23
0.250	3.41±0.07	0.250	2.78±0.20	0.250	6.39±0.16
0.300	2.37±0.07	0.300	1.99±0.20	0.300	4.01±0.12
0.350	1.59±0.04	0.350	1.22±0.11	0.350	2.48±0.08
0.400	1.13±0.05	0.400	0.94±0.11	0.400	1.62±0.09
0.450	0.77±0.03	0.450	0.73±0.11	0.450	1.04±0.05
0.500	0.61±0.03	0.500	0.44±0.07	0.500	0.59±0.05
0.550	0.41±0.02	0.550	0.30±0.06	0.550	0.42±0.05
0.600	0.27±0.02	0.600	0.21±0.07	0.650	0.17±0.01
0.650	0.21±0.02	0.700	0.18±0.03	0.750	0.09±0.01
0.700	0.22±0.03				
0.750	0.10±0.01				
0.800	0.07±0.01				

$\pi^-p\to\pi^-p$		$K^-p\to K^-p$		$\bar{p}p\to\bar{p}p$	
$-t$ (GeV^2)	$d\sigma/dt$ (mb/GeV^2)	$-t$ (GeV^2)	$d\sigma/dt$ (mb/GeV^2)	$-t$ (GeV^2)	$d\sigma/dt$ (mb/GeV^2)
0.0375	22.62±0.43	0.0750	12.07±1.18	0.0375	60.34±1.03
0.075	15.40±0.20	0.110	8.77±1.42	0.075	40.34±0.67
0.110	11.15±0.24	0.130	7.07±0.45	0.110	26.37±0.91
0.130	9.31±0.16	0.170	4.89±0.67	0.130	20.17±1.09
0.150	7.81±0.15	0.200	4.28±0.32	0.150	17.31±0.87
0.170	6.72±0.17	0.250	2.48±0.22	0.170	13.06±0.57
0.200	5.34±0.15	0.300	1.93±0.21	0.200	8.28±0.50
0.250	3.31±0.08	0.350	1.18±0.16	0.250	4.95±0.25
0.300	2.16±0.06	0.400	0.63±0.12	0.300	2.79±0.18
0.350	1.51±0.05	0.450	0.42±0.19	0.350	1.75±0.18
0.400	1.14±0.05	0.500	0.52±0.06	0.400	0.96±0.09
0.450	0.76±0.04	0.600	0.26±0.05	0.450	0.98±0.25
0.500	0.62±0.04	0.650	0.19±0.04	0.500	0.42±0.06
0.550	0.38±0.02	0.750	0.10±0.02	0.550	0.25±0.04
0.600	0.29±0.02			0.600	0.21±0.04
0.650	0.20±0.02			0.650	0.13±0.03
0.700	0.17±0.01			0.750	0.05±0.01
0.750	0.12±0.01				

b. 70 GeV/c

$\pi^+p\to\pi^+p$		$K^+p\to K^+p$		$pp\to pp$	
$-t$ (GeV^2)	$d\sigma/dt$ (mb/GeV^2)	$-t$ (GeV^2)	$d\sigma/dt$ (mb/GeV^2)	$-t$ (GeV^2)	$d\sigma/dt$ (mb/GeV^2)
0.0375	20.57±0.57	0.0375	13.20±0.53	0.0375	52.04±1.08
0.075	14.66±0.24	0.075	9.27±0.31	0.075	34.42±0.42
0.110	10.59±0.23	0.110	7.34±0.30	0.110	24.00±0.49
0.130	9.06±0.22	0.130	6.45±0.45	0.130	19.58±0.43
0.150	7.61±0.19	0.150	5.37±0.28	0.150	15.96±0.36
0.170	6.58±0.20	0.170	4.69±0.51	0.170	13.24±0.44
0.200	5.29±0.15	0.200	3.75±0.20	0.200	10.26±0.31
0.250	3.58±0.12	0.250	2.79±0.21	0.250	6.13±0.21
0.300	2.45±0.06	0.300	1.96±0.14	0.300	3.06±0.10

TABLE IV. (*Continued*)

b. 70 GeV/c

$\pi^+p \to \pi^+p$		$K^+p \to K^+p$		$pp \to pp$	
$-t$ (GeV^2)	$d\sigma/dt$ (mb/GeV^2)	$-t$ (GeV^2)	$d\sigma/dt$ (mb/GeV^2)	$-t$ (GeV^2)	$d\sigma/dt$ (mb/GeV^2)
0.350	1.70 ± 0.04	0.350	1.27 ± 0.10	0.350	2.27 ± 0.06
0.400	1.23 ± 0.03	0.400	1.02 ± 0.08	0.400	1.49 ± 0.04
0.450	0.81 ± 0.02	0.450	0.57 ± 0.07	0.450	0.95 ± 0.04
0.500	0.60 ± 0.02	0.500	0.58 ± 0.05	0.500	0.60 ± 0.03
0.550	0.41 ± 0.02	0.550	0.32 ± 0.07	0.550	0.44 ± 0.03
0.600	0.29 ± 0.02	0.600	0.38 ± 0.08	0.600	0.25 ± 0.04
0.650	0.24 ± 0.03	0.650	0.28 ± 0.07	0.650	0.16 ± 0.02
0.700	0.16 ± 0.01			0.700	0.11 ± 0.01

$\pi^-p \to \pi^-p$		$K^-p \to K^-p$		$\bar{p}p \to \bar{p}p$	
$-t$ (GeV^2)	$d\sigma/dt$ (mb/GeV^2)	$-t$ (GeV^2)	$d\sigma/dt$ (mb/GeV^2)	$-t$ (GeV^2)	$d\sigma/dt$ (mb/GeV^2)
0.0375	20.69 ± 0.34	0.0375	15.27 ± 0.44	0.0375	54.84 ± 0.88
0.075	14.67 ± 0.23	0.075	10.66 ± 0.31	0.075	34.40 ± 0.68
0.110	10.91 ± 0.24	0.110	8.19 ± 0.41	0.110	22.82 ± 0.68
0.130	9.32 ± 0.17	0.130	6.31 ± 0.51	0.130	18.02 ± 0.84
0.150	7.67 ± 0.17	0.150	6.52 ± 0.33	0.150	14.27 ± 0.57
0.170	6.65 ± 0.16	0.170	4.10 ± 0.39	0.170	11.11 ± 0.61
0.200	5.14 ± 0.12	0.200	4.05 ± 0.22	0.200	8.49 ± 0.43
0.250	3.41 ± 0.08	0.250	2.73 ± 0.22	0.250	4.60 ± 0.28
0.300	2.35 ± 0.07	0.300	2.07 ± 0.17	0.300	2.68 ± 0.19
0.350	1.66 ± 0.05	0.350	1.23 ± 0.13	0.350	1.38 ± 0.14
0.400	1.15 ± 0.04	0.400	0.67 ± 0.17	0.400	0.79 ± 0.12
0.450	0.75 ± 0.04	0.450	0.61 ± 0.08	0.450	0.69 ± 0.23
0.500	0.52 ± 0.04			0.500	0.36 ± 0.07

c. 100 GeV/c

$\pi^+p \to \pi^+p$		$K^+p \to K^+p$		$pp \to pp$	
$-t$ (GeV^2)	$d\sigma/dt$ (mb/GeV^2)	$-t$ (GeV^2)	$d\sigma/dt$ (mb/GeV^2)	$-t$ (GeV^2)	$d\sigma/dt$ (mb/GeV^2)
0.110	10.35 ± 0.53	0.075	9.40 ± 1.50	0.0375	48.07 ± 5.10
0.130	9.31 ± 0.38	0.110	8.93 ± 0.98	0.075	28.92 ± 1.61
0.150	7.80 ± 0.20	0.130	6.25 ± 0.53	0.110	22.94 ± 0.68
0.170	6.43 ± 0.21	0.170	4.37 ± 0.70	0.130	18.95 ± 0.46
0.200	4.89 ± 0.16	0.200	3.78 ± 0.42	0.150	15.42 ± 0.24
0.250	3.43 ± 0.11	0.250	3.06 ± 0.20	0.170	12.38 ± 0.24
0.300	2.42 ± 0.10	0.300	2.08 ± 0.25	0.200	9.30 ± 0.19
0.350	1.66 ± 0.07	0.350	1.74 ± 0.26	0.250	5.60 ± 0.12
0.400	1.11 ± 0.05	0.400	1.05 ± 0.09	0.300	3.40 ± 0.10
0.450	0.75 ± 0.05	0.500	0.68 ± 0.08	0.350	2.01 ± 0.06
0.500	0.60 ± 0.04	0.550	0.49 ± 0.08	0.400	1.31 ± 0.05
0.550	0.44 ± 0.04	0.650	0.23 ± 0.02	0.450	0.89 ± 0.04
0.600	0.29 ± 0.02	0.750	0.17 ± 0.03	0.500	0.51 ± 0.04
0.650	0.19 ± 0.01			0.550	0.31 ± 0.04
0.700	0.19 ± 0.02			0.600	0.21 ± 0.01
0.750	0.10 ± 0.01			0.650	0.14 ± 0.01
0.800	0.08 ± 0.01			0.700	0.07 ± 0.02
				0.750	0.05 ± 0.01

TABLE IV. (*Continued*)

c. 100 GeV/c

$\pi^- p \to \pi^- p$		$K^- p \to K^- p$		$\bar{p}p \to \bar{p}p$	
$-t$ (GeV^2)	$d\sigma/dt$ (mb/GeV^2)	$-t$ (GeV^2)	$d\sigma/dt$ (mb/GeV^2)	$-t$ (GeV^2)	$d\sigma/dt$ (mb/GeV^2)
0.0375	21.62±0.44	0.0375	13.37±1.23	0.0375	62.21±3.80
0.075	14.04±0.21	0.075	10.07±0.62	0.075	36.91±1.85
0.110	10.40±0.21	0.110	9.83±0.82	0.110	24.01±1.89
0.130	8.88±0.24	0.130	7.69±0.92	0.130	18.94±1.94
0.150	7.05±0.23	0.150	4.89±0.56	0.150	15.56±1.10
0.170	6.22±0.21	0.170	4.84±0.57	0.170	11.58±1.38
0.200	5.12±0.14	0.200	3.95±0.32	0.200	10.38±0.98
0.250	3.32±0.09	0.250	2.80±0.41	0.250	4.85±0.82
0.300	2.25±0.09	0.300	1.94±0.18	0.300	2.93±0.29
0.350	1.53±0.06	0.350	0.92±0.23	0.350	1.57±0.39
0.400	1.12±0.04	0.400	0.90±0.11	0.400	0.92±0.17
0.450	0.73±0.03	0.450	0.61±0.07	0.450	0.59±0.12
0.500	0.54±0.02	0.500	0.51±0.08	0.500	0.30±0.10
0.550	0.38±0.03	0.600	0.18±0.10	0.650	0.11±0.09
0.600	0.23±0.02	0.650	0.20±0.02	0.750	0.14±0.17
0.650	0.20±0.02	0.750	0.08±0.06		
0.700	0.15±0.01				
0.750	0.11±0.01				
0.800	0.08±0.01				

d. 140 GeV/c

$\pi^+ p \to \pi^+ p$		$K^+ p \to K^+ p$		$pp \to pp$	
$-t$ (GeV^2)	$d\sigma/dt$ (mb/GeV^2)	$-t$ (GeV^2)	$d\sigma/dt$ (mb/GeV^2)	$-t$ (GeV^2)	$d\sigma/dt$ (mb/GeV^2)
0.0375	21.37±0.54	0.0750	10.58±0.47	0.0375	51.30±1.39
0.0750	14.84±0.29	0.1100	8.01±0.40	0.0750	32.93±0.62
0.1100	10.53±0.40	0.1300	6.35±0.22	0.1100	23.17±0.87
0.1300	9.11±0.23	0.1500	5.81±0.42	0.1300	17.22±0.45
0.1500	8.03±0.37	0.1700	4.55±0.47	0.1500	14.74±0.69
0.1700	6.75±0.19	0.2000	4.07±0.16	0.1700	11.63±0.34
0.2000	5.19±0.13	0.2500	2.60±0.22	0.2000	8.86±0.24
0.2500	3.49±0.16	0.3000	1.88±0.06	0.2500	5.51±0.26
0.3000	2.35±0.08	0.3500	1.27±0.06	0.3000	3.21±0.10
0.3500	1.67±0.06	0.4000	0.96±0.06	0.3500	2.00±0.07
0.4000	1.11±0.03	0.4500	0.75±0.06	0.4000	1.28±0.03
0.4500	0.78±0.03	0.5000	0.52±0.04	0.4500	0.79±0.03
0.5000	0.55±0.02	0.5500	0.35±0.05	0.5000	0.54±0.02
0.5500	0.43±0.03	0.6000	0.29±0.03	0.5500	0.35±0.02
0.6000	0.27±0.02	0.6500	0.24±0.05	0.6000	0.21±0.01
0.6500	0.19±0.02	0.7000	0.15±0.02	0.6500	0.13±0.01
0.7000	0.18±0.02			0.7000	0.09±0.01
0.7500	0.13±0.02			0.7500	0.06±0.01
0.8000	0.09±0.01			0.8000	0.06±0.01

$\pi^- p \to \pi^- p$		$K^- p \to K^- p$		$\bar{p}p \to \bar{p}p$	
$-t$ (GeV^2)	$d\sigma/dt$ (mb/GeV^2)	$-t$ (GeV^2)	$d\sigma/dt$ (mb/GeV^2)	$-t$ (GeV^2)	$d\sigma/dt$ (mb/GeV^2)
0.0375	20.98±0.55	0.0750	11.03±0.45	0.0750	36.06±1.42
0.0750	14.88±0.23	0.1100	7.32±0.56	0.1100	24.12±2.02
0.1100	10.41±0.23	0.1300	6.73±0.26	0.1300	17.54±1.15
0.1300	9.24±0.25	0.1500	5.66±0.28	0.1500	14.50±0.84
0.1500	7.44±0.20	0.1700	4.91±0.55	0.1700	13.48±1.58
0.1700	6.68±0.18	0.2000	4.04±0.20	0.2000	8.52±1.04
0.2000	5.17±0.13	0.2500	2.81±0.21	0.2500	5.03±0.54
0.2500	3.42±0.14	0.3000	1.89±0.14	0.3500	1.61±0.60
0.3000	2.34±0.08	0.3500	1.08±0.24	0.4000	1.26±0.17
0.3500	1.41±0.07	0.4000	0.84±0.05	0.5000	0.35±0.13

TABLE IV. (*Continued*)

d. 140 GeV/c

$\pi^-p \to \pi^-p$		$K^-p \to K^-p$		$\bar{p}p \to \bar{p}p$	
$-t$ (GeV^2)	$d\sigma/dt$ (mb/GeV^2)	$-t$ (GeV^2)	$d\sigma/dt$ (mb/GeV^2)	$-t$ (GeV^2)	$d\sigma/dt$ (mb/GeV^2)
0.4000	1.15 ± 0.06	0.4500	0.26 ± 0.17	0.6000	0.22 ± 0.10
0.4500	0.76 ± 0.06	0.5000	0.43 ± 0.05		
0.5000	0.48 ± 0.04	0.6000	0.23 ± 0.05		
0.5500	0.39 ± 0.02				
0.6000	0.27 ± 0.03				
0.6500	0.16 ± 0.02				
0.7000	0.15 ± 0.01				
0.7500	0.12 ± 0.01				

e. 175 GeV/c

$\pi^+p \to \pi^+p$		$K^+p \to K^+p$		$pp \to pp$	
$-t$ (GeV^2)	$d\sigma/dt$ (mb/GeV^2)	$-t$ (GeV^2)	$d\sigma/dt$ (mb/GeV^2)	$-t$ (GeV^2)	$d\sigma/dt$ (mb/GeV^2)
0.075	14.96 ± 0.16	0.0375	14.54 ± 0.33	0.075	33.12 ± 0.46
0.110	10.84 ± 0.17	0.075	10.65 ± 0.22	0.110	24.22 ± 0.64
0.130	9.18 ± 0.12	0.110	8.19 ± 0.31	0.150	15.06 ± 0.47
0.150	7.73 ± 0.14	0.130	6.68 ± 0.24	0.170	11.30 ± 0.42
0.170	6.30 ± 0.19	0.150	5.81 ± 0.26	0.200	8.54 ± 0.38
0.200	5.07 ± 0.07	0.170	4.58 ± 0.38	0.250	5.27 ± 0.05
0.250	3.50 ± 0.04	0.200	3.98 ± 0.19	0.300	3.22 ± 0.06
0.300	2.31 ± 0.04	0.250	2.69 ± 0.06	0.350	2.07 ± 0.04
0.350	1.57 ± 0.04	0.300	2.06 ± 0.09	0.400	1.24 ± 0.03
0.400	1.09 ± 0.03	0.350	1.32 ± 0.05	0.450	0.75 ± 0.03
0.450	0.78 ± 0.03	0.400	0.95 ± 0.06	0.500	0.48 ± 0.03
0.500	0.60 ± 0.03	0.450	0.65 ± 0.06	0.550	0.28 ± 0.02
0.550	0.39 ± 0.02	0.500	0.56 ± 0.05	0.600	0.23 ± 0.02
0.600	0.30 ± 0.02	0.550	0.41 ± 0.03	0.650	0.13 ± 0.01
0.650	0.20 ± 0.01	0.600	0.30 ± 0.03	0.750	0.06 ± 0.01
0.700	0.16 ± 0.01	0.650	0.19 ± 0.03		
0.750	0.11 ± 0.01	0.750	0.10 ± 0.01		
0.800	0.08 ± 0.01				

$\pi^-p \to \pi^-p$		$K^-p \to K^-p$		$\bar{p}p \to \bar{p}p$	
$-t$ (GeV^2)	$d\sigma/dt$ (mb/GeV^2)	$-t$ (GeV^2)	$d\sigma/dt$ (mb/GeV^2)	$-t$ (GeV^2)	$d\sigma/dt$ (mb/GeV^2)
0.0375	24.30 ± 1.08	0.075	11.42 ± 0.31	0.0375	46.60 ± 5.68
0.075	15.60 ± 0.29	0.110	7.65 ± 0.59	0.075	32.95 ± 1.22
0.110	11.28 ± 0.38	0.130	6.12 ± 0.54	0.110	25.06 ± 2.39
0.130	8.83 ± 0.23	0.150	6.14 ± 0.17	0.130	16.07 ± 2.12
0.150	7.37 ± 0.11	0.170	4.80 ± 0.34	0.150	13.99 ± 0.49
0.170	6.17 ± 0.15	0.200	3.88 ± 0.12	0.170	9.85 ± 1.19
0.200	4.98 ± 0.12	0.250	2.67 ± 0.13	0.200	7.66 ± 0.33
0.250	3.29 ± 0.08	0.300	2.09 ± 0.24	0.250	4.03 ± 0.63
0.300	2.19 ± 0.03	0.350	1.21 ± 0.06	0.350	1.65 ± 0.11
0.350	1.52 ± 0.05	0.400	0.83 ± 0.10	0.400	1.01 ± 0.31
0.400	1.03 ± 0.03	0.450	0.60 ± 0.06	0.450	0.52 ± 0.33
0.450	0.73 ± 0.03	0.500	0.40 ± 0.10	0.500	0.39 ± 0.36
0.500	0.53 ± 0.02	0.600	0.26 ± 0.03	0.600	0.16 ± 0.07
0.550	0.38 ± 0.01	0.650	0.09 ± 0.09		
0.600	0.25 ± 0.01	0.750	0.09 ± 0.09		
0.650	0.19 ± 0.01				
0.700	0.16 ± 0.01				
0.750	0.09 ± 0.01				
0.800	0.08 ± 0.01				

TABLE V. Quadratic-exponential fits: Fits of cross sections from Table IV to $d\sigma/dt = Ae^{B|t|+Ct^2}$. The optical-theorem prediction (OTP) is included as a data point with a 3% uncertainty. $P(\chi^2)$ is the probability of getting a χ^2 greater than the value observed. "degf" is the number of degrees of freedom.

	p (GeV/c)	OTP (mb/GeV^2)	A (mb/GeV^2)	B (GeV^{-2})	C (GeV^{-4})	$B(-0.2)$ (GeV^2)	$P(\chi^2)$	degf
π^-p	50	29.5	31.3±0.4	−9.7±0.1	3.1±0.2	−8.45±0.06	0.09	16
	70	29.4	28.9±0.5	−9.1±0.2	2.4±0.4	−8.14±0.06	0.90	11
	100	29.3	28.5±0.4	−9.2±0.1	2.4±0.2	−8.27±0.06	0.01	17
	140	29.6	29.2±0.5	−9.2±0.2	2.4±0.3	−8.28±0.07	0.22	16
	175	29.9	30.2±0.5	−9.6±0.1	2.8±0.2	−8.46±0.06	0.00	17
K^-p	50	21.0	21.2±0.6	−8.9±0.3	2.5±0.6	−7.95±0.14	0.51	12
	70	21.0	20.9±0.5	−8.8±0.4	2.2±1.1	−7.92±0.17	0.10	10
	100	21.3	21.0±0.6	−9.0±0.4	2.8±0.7	−7.93±0.14	0.28	14
	140	21.6	21.4±0.6	−9.1±0.3	2.4±0.7	−8.07±0.13	0.53	11
	175	21.9	22.2±0.6	−9.2±0.3	2.8±0.5	−8.11±0.10	0.68	13
$\bar{p}p$	50	98.3	99.2±1.7	−12.6±0.2	3.3±0.5	−11.34±0.10	0.26	15
	70	94.0	89.5±1.8	−12.8±0.3	3.4±1.0	−11.46±0.15	0.61	11
	100	90.3	91.3±2.5	−11.9±0.5	1.4±1.3	−11.38±0.22	0.86	13
	140	88.9	89.3±2.6	−12.6±0.4	4.0±1.2	−10.97±0.24	0.93	10
	175	88.4	87.4±2.4	−13.1±0.4	4.7±1.1	−11.20±0.19	0.90	12
π^+p	50	27.4	27.3±0.4	−8.7±0.1	1.8±0.2	−8.01±0.06	0.25	17
	70	27.4	27.3±0.5	−8.6±0.1	1.9±0.3	−7.86±0.06	0.79	15
	100	27.7	27.5±0.7	−8.8±0.2	2.0±0.3	−8.00±0.09	0.60	15
	140	28.0	28.8±0.5	−9.0±0.1	2.2±0.2	−8.11±0.06	0.80	17
	175	28.5	28.8±0.4	−9.1±0.1	2.3±0.2	−8.15±0.05	0.49	16
K^+p	50	16.6	16.6±0.4	−7.6±0.3	1.1±0.6	−7.13±0.12	0.66	14
	70	17.2	17.3±0.4	−8.1±0.3	2.2±0.6	−7.20±0.11	0.61	14
	100	18.2	18.0±0.5	−7.8±0.3	1.9±0.5	−7.03±0.13	0.62	11
	140	18.9	18.7±0.5	−8.3±0.2	2.2±0.4	−7.44±0.09	0.34	15
	175	19.7	19.7±0.3	−8.4±0.2	2.1±0.3	−7.56±0.07	0.56	15
pp	50	76.2	75.9±0.9	−10.3±0.1	1.5±0.3	−9.67±0.06	0.99	14
	70	75.8	75.6±1.1	−10.6±0.2	1.8±0.3	−9.81±0.06	0.85	15
	100	75.9	73.6±1.7	−10.7±0.2	1.5±0.3	−10.09±0.08	0.47	16
	140	76.3	75.7±1.3	−11.3±0.1	2.5±0.2	−10.25±0.06	0.53	17
	175	76.8	76.5±1.3	−11.3±0.1	2.3±0.2	−10.32±0.05	0.09	13

sections on a finer grid indicate that no structure is lost because of this binning.) The smooth curves in Fig. 10 were obtained from the fits described below.

A. Parametrization of the data

Fits of the form $d\sigma/dt = Ae^{B|t|+C|t|^2}$ (quadratic exponential) were found to give a good representation of the data over the whole t range. This form was proposed on theoretical grounds by Van Hove.[17] Parameters obtained from the fits are presented in Table V. Only statistical uncertainties on the data points have been included in the fits.

The "slope parameter" or logarithmic derivative, $B(t)$, is defined as

$$B(t) = d/d|t| \ \ln d\sigma/dt = B + 2C|t| . \quad (4)$$

The value of $B(-0.2)$, as calculated from the fit, is also shown.

The fits presented have the optical-theorem prediction included as a data point with ±3% uncertainty. This is done to help reduce the strong correlation between the A, B, and C parameters. The results do not change appreciably if the uncertainty is reduced to 2% or 1%, or if the optical point is entirely excluded from the fit.

The optical-theorem prediction (OTP) is listed for each reaction in Table V. These values have been computed using recent Fermilab total-cross-section measurements,[15] with the small effect of the real part included. The ratio of the real to imaginary part for proton-proton scattering has been measured by the U.S.A.-U.S.S.R. collaboration at Fermilab.[18] For other reactions, theoretical calculations[19] based on dispersion relations have been used. All these values agree well with the preliminary results of Fermilab experiment 69.[20]

The χ^2 probability and the number of degrees of freedom are given in the last two columns of Table V. Table VI gives the full error matrix for each fit.

The possibility of other paremetrizations, such as piecewise fits with simple exponential is discussed below.

The systematic uncertainties, discussed above, frequently dominate the statistical uncertainties given in Table V, especially for protons and pions. The systematic errors are ±3% on the absolute normalization, ±1.5% on B and $B(-0.2)$, and ±3% on C. To check that the slope parameters are not influenced by the systematic errors which come in at large t, fits were also done using only the data at $|t| \leq 0.4$ GeV^2. The slope parameters obtained are consistent with the ones from the fits to the full t range.

Figure 11 shows the ratio of the A parameters (obtained from fits which did not include the optical points) to the optical point for all 30 fits. These plots show that the absolute normalization is consistent with the optical-theorem predictions within the stated systematic and statistical errors.

B. Total elastic cross sections

Table VII presents the total elastic cross sections σ_{el}, as calculated for each reaction from the fits of Table V according to the formula

$$\sigma_{el} = \int_{0.0}^{0.8} A\, e^{B|t|+C|t|^2} d|t| . \quad (5)$$

Contributions from $|t| > 0.8$ GeV^2 are less than 0.5% since the elastic cross section has fallen by more than two orders of magnitude from its value

TABLE VI. Error matrices for fits of Table V. $\sigma_{AA}{}^2$, $\sigma_{BB}{}^2$, and $\sigma_{CC}{}^2$ are the mean-squared uncertainties of the best-fit values A, B, and C, respectively. σ_{AB}, σ_{AC}, and σ_{BC} are the average values of the quantities AB, AC, and BC, respectively. They reflect the correlations between the parameters introduced by the fitting procedure.

	p (GeV/c)	$\sigma_{AA}{}^2$ (mb^2/GeV^4)	$\sigma_{BB}{}^2$ (GeV^{-4})	$\sigma_{CC}{}^2$ (GeV^{-8})	σ_{AB} (mb/GeV^4)	σ_{AC} (mb/GeV^6)	σ_{BC} (1/GeV^6)
π^-p	50	0.17	0.01	0.02	−0.04	0.05	−0.02
	70	0.22	0.04	0.19	−0.08	0.15	−0.08
	100	0.18	0.02	0.05	−0.05	0.07	−0.03
	140	0.25	0.03	0.07	−0.07	0.10	−0.04
	175	0.26	0.01	0.03	−0.05	0.06	−0.02
K^-p	50	0.37	0.11	0.36	−0.11	0.14	−0.18
	70	0.26	0.15	1.15	−0.15	0.33	−0.38
	100	0.34	0.12	0.43	−0.12	0.17	−0.21
	140	0.36	0.11	0.53	−0.15	0.25	−0.22
	175	0.32	0.06	0.27	−0.12	0.18	−0.12
$\bar{p}p$	50	2.83	0.05	0.24	−0.31	0.52	−0.10
	70	3.06	0.11	0.94	−0.48	1.15	−0.29
	100	6.31	0.22	1.73	−0.75	1.46	−0.56
	140	6.51	0.19	1.50	−0.75	1.38	−0.46
	175	5.92	0.14	1.21	−0.66	1.29	−0.38
π^+p	50	0.16	0.02	0.04	−0.04	0.05	−0.02
	70	0.20	0.02	0.07	−0.06	0.08	−0.04
	100	0.50	0.03	0.07	−0.11	0.14	−0.05
	140	0.24	0.02	0.06	−0.06	0.08	−0.03
	175	0.15	0.01	0.03	−0.04	0.05	−0.02
K^+p	50	0.17	0.09	0.36	−0.09	0.13	−0.17
	70	0.18	0.09	0.41	−0.10	0.16	−0.18
	100	0.28	0.10	0.27	−0.09	0.11	−0.15
	140	0.22	0.05	0.16	−0.08	0.11	−0.08
	175	0.12	0.03	0.08	−0.04	0.06	−0.04
pp	50	0.87	0.02	0.07	−0.11	0.18	−0.03
	70	1.29	0.02	0.09	−0.15	0.25	−0.04
	100	2.78	0.03	0.09	−0.27	0.38	−0.05
	140	1.72	0.02	0.06	−0.16	0.22	−0.03
	175	1.74	0.02	0.06	−0.15	0.23	−0.03

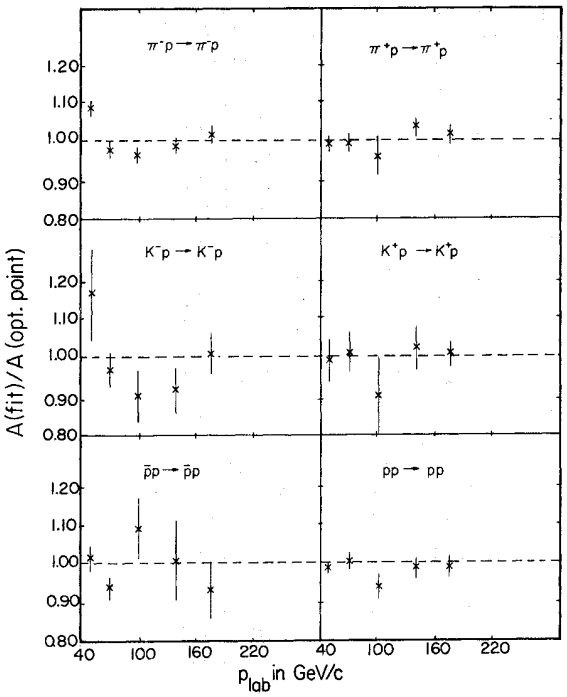

FIG. 11. Comparison of the A parameters from the quadratic exponential fits without the optical-point constraint to the optical-theorem predictions.

at $t=0$. The result is, however, sensitive to the extrapolation of the measured cross section to $t=0$. Typically, (15–20)% of σ_{el} comes from this extrapolation at the low energies (50 and 70 GeV) and (35–45)% comes from this extrapolation at the higher energies. The use of the optical-theorem point as a constraint in the fitting procedure helps to reduce errors from this source. Systematic uncertainties of ±2% were added in quadrature with the statistical errors to account for uncertainties in the overall normalization, errors in the extrapolation to $t=0$, and the effect of contributions from large-t values.

Table VII also includes values of the total cross sections, σ_{tot}, obtained from Ref. 15, the total inelastic cross section $\sigma_{inel}=\sigma_{tot}-\sigma_{el}$, and the ratio of the total elastic to the total cross section. For the purposes of the uncertainty calculation, errors of 0.5% have been assigned to the total cross sections.

VII. COMPARISON OF RESULTS WITH OTHER EXPERIMENTS

In this section, the results are compared with the results from experiments at nearby energies. The relation between these results and data at lower energies (<40 GeV/c) and higher energies, including CERN ISR energies (290–1480 GeV equivalent laboratory energy), is discussed later in the context of the energy dependence of elastic scattering.

Figure 12 shows the ratio of these results on π^-p, K^-p, and $p\bar{p}$ scattering to the fits of Antipov *et al.*,[21] at 40 GeV/c. Figure 13 compares π^-p at 50 GeV/c to the measurement of Derevchekov *et al.*[22] The only significant disagreement seems to be with Derevchekov at $-t \gtrsim 0.3$ GeV^2. The agreement with Antipov in this region is good.

Figure 14 compares proton data with the small $-t$ ($-t \lesssim 0.15$ GeV^2) measurements of the Fermilab U.S.A.-U.S.S.R.) collaboration.[23] In general, our slopes at small $-t$ are typically (2 to 3)% lower than the USA-USSR slopes and 5% lower at 50 GeV/c. This may reflect the 1.5% systematic errors in our data, the 0.15-GeV^{-2} energy-independent systematic error of their experiment, or it may reflect the different t ranges covered by the two experiments. Finally, Fig. 15 shows data from Fermilab experiment 7,[24] plotted relative to the fits of this experiment.

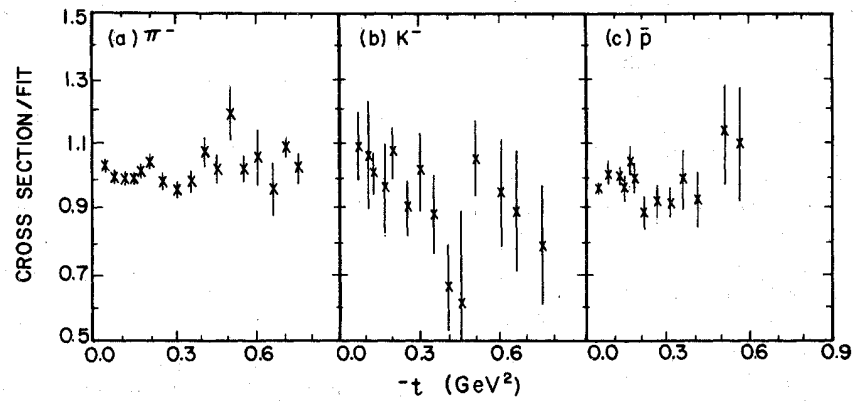

FIG. 12. Comparison of the results from this experiment with the results of Antipov *et al.* (Ref. 21) at 40 GeV/c. Plotted are the data points of this experiment divided by the quadratic exponential fits of Ref. 21.

TABLE VII. Total elastic cross sections calculated from fit of Tables V and VI.

	p (GeV/c)	σ_{el} (mb)	σ_{tot} (mb)	σ_{inel} (mb)	$\frac{\sigma_{el}}{\sigma_{tot}}$
π^+p	50	3.29±0.11	23.07±0.12	19.78±0.16	0.142±0.005
	70	3.35±0.12	23.16±0.12	19.81±0.17	0.145±0.005
	100	3.30±0.15	23.29±0.12	19.99±0.19	0.142±0.007
	140	3.39±0.12	23.43±0.12	20.04±0.17	0.145±0.005
	175	3.37±0.10	23.60±0.12	20.23±0.16	0.143±0.004
K^+p	50	2.27±0.09	18.03±0.09	15.76±0.13	0.126±0.005
	70	2.30±0.10	18.36±0.09	16.06±0.14	0.125±0.005
	100	2.47±0.11	18.85±0.09	16.38±0.15	0.131±0.006
	140	2.40±0.10	19.23±0.10	16.83±0.14	0.125±0.005
	175	2.50±0.08	19.59±0.10	17.09±0.13	0.128±0.004
pp	50	7.61±0.29	38.14±0.19	30.53±0.35	0.199±0.008
	70	7.41±0.31	38.24±0.19	30.83±0.37	0.194±0.008
	100	7.07±0.35	38.39±0.19	31.32±0.40	0.184±0.009
	140	7.00±0.28	38.57±0.19	31.57±0.34	0.182±0.007
	175	7.06±0.28	38.76±0.19	31.70±0.34	0.182±0.007
π^-p	50	3.48±0.11	24.01±0.12	20.53±0.16	0.145±0.005
	70	3.39±0.14	24.00±0.12	20.61±0.19	0.141±0.006
	100	3.28±0.11	23.96±0.12	20.68±0.16	0.137±0.005
	140	3.36±0.12	24.00±0.12	20.64±0.17	0.140±0.005
	175	3.38±0.11	24.17±0.12	20.79±0.17	0.140±0.005
K^-p	50	2.54±0.11	20.25±0.10	17.71±0.15	0.125±0.006
	70	2.53±0.12	20.30±0.10	17.77±0.16	0.125±0.006
	100	2.51±0.12	20.41±0.10	17.90±0.16	0.123±0.006
	140	2.52±0.12	20.50±0.10	17.98±0.16	0.123±0.006
	175	2.59±0.12	20.70±0.10	18.11±0.16	0.125±0.006
$\bar{p}p$	50	8.20±0.40	43.86±0.22	35.66±0.45	0.187±0.009
	70	7.30±0.47	43.00±0.22	35.70±0.52	0.170±0.011
	100	7.80±0.60	42.04±0.21	34.24±0.63	0.185±0.014
	140	7.52±0.60	41.80±0.21	34.28±0.63	0.180±0.014
	175	7.12±0.52	41.60±0.21	34.48± 0.56	0.171±0.013

VIII. DISCUSSION

A. t dependence

The cross sections are quite well described by the quadratic-exponential form over the whole t range from -0.04 to -0.80 GeV^2. No dips are observed within the limits of the t resolution. The C parameters of ~2 GeV^{-4} imply a linear change in slope of $2C\Delta t$ or about 1.6 GeV^{-2} from $-t=0.1$ to $-t=0.5$. Experiments on p-p elastic scattering at ISR[25] suggest that this change in slope does not occur linearly but occurs abruptly in the neighborhood of $-t=0.15$ GeV^2. The existence of such a "break" had been proposed prior to this by Carrigan.[26] Table VIII shows the results of simple exponential fits to data in the two intervals $0.037<-t<0.13$ GeV^2 and $0.16<-t<0.50$ GeV^2 for pp and π^+p. These fits are consistent with the break hypothesis. The success of the two parametrizations indicates that the data lack the statistical precision

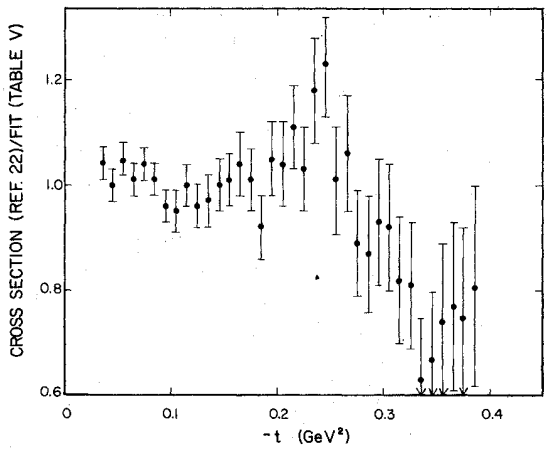

FIG. 13. Comparison of the results of this experiment to the results of Derevchekov *et al.* (Ref. 22) at 50 GeV/c for $\pi^-p\to\pi^-p$. The ratio of their data points to the fitted values from Table V are plotted.

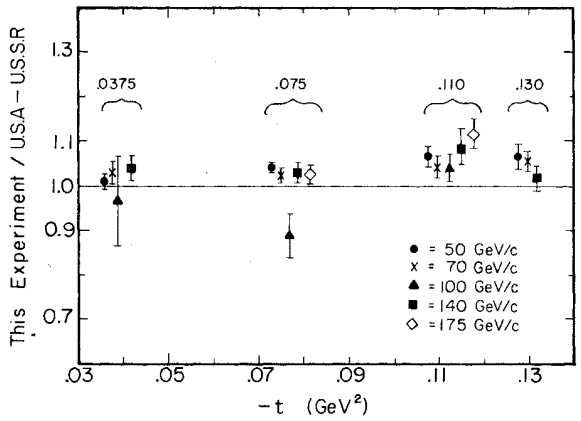

FIG. 14. Comparison of pp elastic scattering results from this experiment to the results of the U.S.A-U.S.S.R. collaboration at Fermilab (Ref. 23). The slope parameter B from Ref. 23 has been used to calculate cross-section values according to the formula $d\sigma/dt = Ae^{Bt}$, where A is the optical-theorem prediction. The ratios of the measured cross section from this experiment to the cross sections calculated as described are plotted.

to distinguish between them. It is estimated that at least one million events in a t interval from -0.04 to -0.25 GeV^2 would be required to resolve this matter. A recent, high-statistics experiment[27] in the 10- to 14-GeV/c range has also observed structure in the low-t cross sections for the other channels. More precise experiments are clearly required.

B. Energy dependence of the B and C parameters

Figure 16 shows the energy dependence of the B and C parameters[28] from 10 GeV to the highest energies available. Detailed comparisons are difficult because the various experiments cover different t ranges, use different fitting procedures, and treat systematic errors in different ways. The B and C parameters are also highly correlated by the fits. In spite of these problems, the following conclusions emerge:

(i) pp and K^+p elastic scatterings show pronounced "shrinkage" of the B parameter.

(ii) The B parameters for π^-p, π^+p, and K^-p show little energy dependence above 10 GeV.

(iii) Above 10 GeV, a C parameter of approximately 2 GeV^{-4} is required by the fit in all reactions. A C parameter of 2 implies a strongly curved $\ln d\sigma/dt$. If one extrapolated the low-t cross section $|t|<0.1$ to $|t|\simeq 0.8$, one would be incorrect by a factor of ~4.

The fact that the logarithmic derivative varies in t (because $C\neq 0$) as well as in s means that one must use data taken in the same t range to study

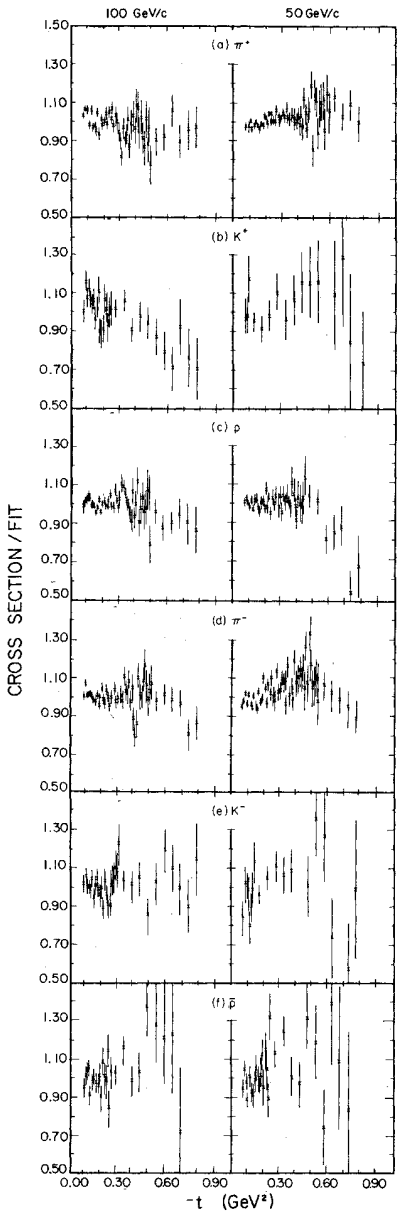

FIG. 15. Ratio of cross sections from Akerlof *et al.* (Ref. 24) to fits of Table V. Absolute normalization differences have been removed before computing these ratios.

the s dependence.

The slope parameters at $-t=0.2$ GeV^2 are plotted in Fig. 17 against s. These parameters are less sensitive to the fitting interval than B or C individually and the effect of the correlation between B and C is reduced. There is less energy dependence at $-t=0.2$ GeV^2 than at $t=0$ and the protons seem to achieve by 175 GeV/c a value which is close to that observed across the whole ISR range. $B(-0.2)$

TABLE VIII. Piecewise exponential parametrization of π^+p and pp elastic scattering: $d\sigma/dt = Ae^{B|t|}$. $P(\chi^2)$ is probability of getting a χ^2 greater than the value observed.

		$0.037 \le \lvert t \rvert \le 0.13$ GeV^2			$0.16 \le \lvert t \rvert \le 0.50$ GeV^2		
	p (GeV/c)	A (mb/GeV^2)	B (GeV^{-2})	$P(\chi^2)$	A (mb/GeV^2)	B (GeV^{-2})	$P(\chi^2)$
π^+p	50	28.2±0.8	−8.9±0.3	0.24	22.2±0.9	−7.4±0.1	0.18
π^+p	70	28.7±1.0	−9.0±0.4	0.77	22.5±0.8	−7.3±0.1	0.65
π^+p	140	30.0±1.0	−9.3±0.4	0.58	24.0±0.8	−7.6±0.1	0.66
pp	50	75.3±1.5	−10.0±0.2	0.86	67.5±2.6	−9.4±0.1	0.87
pp	70	76.3±2.0	−10.5±0.3	0.68	66.4±2.5	−9.5±0.1	0.42
pp	140	79.3±2.7	−11.6±0.4	0.36	58.7±2.1	−9.6±0.1	0.30

for the antiprotons seems to be converging toward the value for the protons but may be leveling off at a slightly larger value.

C. Parametrization of the s dependence by a single-Regge-pole model

If small-t elastic scattering is dominated at high energies by a single effective Regge pole, then the cross section has the form

$$d\sigma/dt = F(t)(s/s_0)^{2\alpha(t)-2}, \tag{6}$$

where $\alpha(t)$ is the trajectory of the moving pole and s_0 is a scale factor, here taken as 188 GeV^2, corresponding to an incident energy of 100 GeV. $F(t)$ is taken to have a quadratic-exponential form:

$$F(t) = A_{s_0} e^{Bs_0|t| + Cs_0|t|^2}. \tag{7}$$

Table IX shows the results of fits to this form for all five energies. No energy-dependent systematic errors are included. To see the effects of energy-dependent systematic errors, a separate fit of the logarithmic slope at $-t = 0.2$ GeV^2 to the form

$$B(t) = B_0(t) + 2\alpha'(t) \ln s/s_0 \tag{8}$$

is presented in Table X. An estimated energy-dependent systematic error of 1% is added in quadrature to the statistical errors on $B(-0.2)$. The errors on the slope parameter α' increase by a factor of 2 owing to systematic errors for π^+, π^-, and p but do not change appreciably for the minority particles K^+, K^-, and $\bar{p}$.

These results confirm the qualitative observations that the pp and K^+p continue to shrink at these energies. The rate of shrinkage α', which is ~0.2 GeV^{-2} for both reactions, is less than the value $\alpha' \approx 0.5$ GeV^{-2} (see Ref. 24) obtained from similar fits to the low-energy data. For $\bar{p}p$, it is clear that the rapid antishrinkage observed at lower energies is also slowing down.

pp and K^+p slopes have similar energy dependences. Duality arguments suggest that pp and K^+p, which have exotic s-channel quantum numbers, will achieve asymptotic behavior—i.e., become dominated by the Pomeron pole—at lower energies than the other four reactions. To check this idea, the proton data at each t value have been fitted to the single-Regge-pole cross section. The resulting trajectory is plotted in Fig. 18 and is indeed compatible with a straight line. The best-fit straight line is

$$\alpha(t) = (0.98 \pm 0.01) - (0.22 \pm 0.03)|t|. \tag{9}$$

This is quite close to the form usually favored for the Pomeron. Obviously, the statistical accuracy is insufficient to rule out other functional forms for $\alpha(t)$.

A major obstacle in the study of the Pomeron has been the difficulty of extracting its exchange amplitude from the data. Unlike amplitudes associated with quantum-number exchange, which can be characterized by a power-law behavior in s, vacuum exchanges have a very complicated energy dependence. A simple interpretation of the vacuum exchange is that it receives contributions from the Pomeron Regge pole with an intercept of ~1 and the f Regge pole with an intercept of ~$\frac{1}{2}$. In an effort to isolate the Pomeron-exchange amplitude, Quigg and Rabinovici[30] have studied the following linear combinations of elastic scattering amplitudes S:

$$S(K^+p) + S(K^-p) - \tfrac{1}{2}[S(\pi^+p) + S(\pi^-p)], \tag{10}$$

which in the quark model corresponds to the ϕp elastic scattering amplitude $S(\phi p)$. An ideally mixed f trajectory does not couple to the strange quarks in the ϕ so that only Pomeron exchange contributes to this amplitude. By use of the optical theorem, one has

$$\sigma_{\text{total}}(\phi p) = \sigma_{\text{total}}(K^+p) + \sigma_{\text{total}}(K^-p) - \tfrac{1}{2}[\sigma_{\text{total}}(\pi^+p) + \sigma_{\text{total}}(\pi^-p)]. \tag{11}$$

This cross section is found to be a linearly rising function of $\ln s$ from an incident momentum of 6 to 200 GeV/c. Following their example, Fig. 19

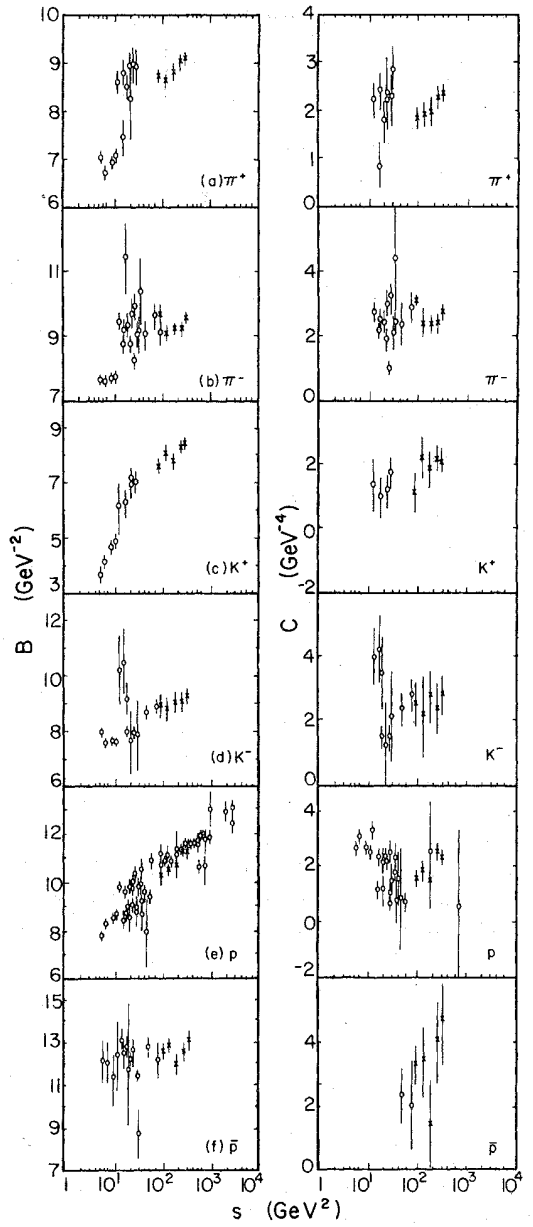

FIG. 16. Energy dependence of B and C parameters from a few GeV to the highest available energies. Circles represent values taken from Ref. 28 and crosses are the values obtained in this experiment. The variable s is $2m_p P_{\text{inc}}$.

shows the quark-model prediction for the "ϕ"p elastic cross section $d\sigma/dt$("ϕ"p),

$$\frac{d\sigma}{dt}(\text{“}\phi\text{”}p) = \frac{d\sigma}{dt}(K^+p) + \frac{d\sigma}{dt}(K^-p) - \frac{1}{2}\left[\frac{d\sigma}{dt}(\pi^+p) + \frac{d\sigma}{dt}(\pi^-p)\right], \tag{12}$$

constructed from the cross sections of Table IV.

These cross sections have been fitted with quadratic exponentials together with the optical point calculated from the $K^{\pm}p$, $\pi^{\pm}p$ total cross sections. A 3% uncertainty was assigned to the optical point. The results of these fits are given in Table XI together with the logarithmic slope at $t = -0.2$ GeV^2. This logarithmic slope is plotted in Fig. 20 as a function of energy and shows clear indications of shrinkage. The solid line corresponds to a Pomeron trajectory with a slope of $\alpha' = 0.2$ GeV^{-2}, consistent with that found in pp and K^+p scattering.

D. Elastic scattering crossovers[2]

Although high-energy elastic scattering is dominated by diffraction, or (in t-channel language) by Pomeron exchange, amplitudes with quantum-number exchange can be isolated by careful comparison of closely related reactions. In particular, the particle-antiparticle elastic cross sections differ from one another because of interference between $C = +1$ and $C = -1$ exchange amplitudes,

$$d\sigma/dt(x^{\pm}p) = |F^+ \mp F^-|^2, \tag{13}$$

where the $F^{\pm}$ amplitudes correspond to $C = \pm 1$ exchange. Since the diffractive amplitude with $C = +1$ dominates, the quantity

$$\Delta = \frac{\sigma^- - \sigma^+}{[8(\sigma^- + \sigma^+)]^{1/2}}, \tag{14}$$

where $\sigma^{\pm} \equiv d\sigma/dt(x^{\pm}p)$, isolates to a good approximation that part of F^- with the same phase and spin state as the $C = +1$ amplitude (mainly imaginary nonflip).[31] For Kp and pp scattering the $C = -1$ amplitude is thought to be dominated by nonflip ω exchange.[31] At momenta $\lesssim 10$ GeV/c, this amplitude changes sign near $-t = 0.2$ GeV^2, resulting in the crossover effect where the differential cross sections for particle and antiparticle scattering are equal.[32,33] The momentum transfer t_c at which this occurs can be related to a typical interaction radius in impact-parameter space for the peripheral $C = -1$ amplitude.[34]

The crossovers were calculated from the fits of Table V. Figure 21 shows the results of the $K^{\pm}p$ and $p^{\pm}p$ fits. In each case a crossover is found consistent with $-t_c$ in the range 0.1 to 0.2 GeV^2, and the values of t_c obtained from the fits are plotted in Fig. 22 as a function of laboratory momentum. For Kp scattering the crossover points are consistent with those found at lower energies,[32,33] with the average being $-t_c = 0.19 \pm 0.04$ GeV^2, where the error includes both statistical and systematic uncertainties. The nucleon values average to $-t_c = 0.11 \pm 0.02$ GeV^2, definitely lower than the value 0.162 ± 0.004 GeV^2 reported[32] near 5 GeV/c.

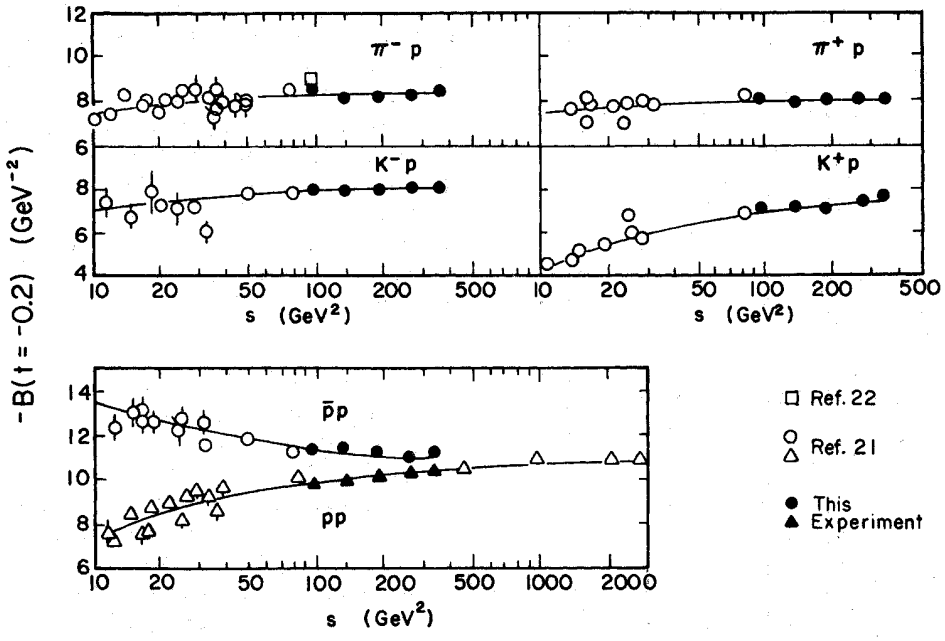

FIG. 17. Slope parameters at $-t = 0.2$ GeV^2 as a function of s.

The energy dependence of Δ for $p^{\pm}p$ scattering has been studied using the form

$$\Delta(t) = c(t)\, s^{\alpha(t)-1}, \tag{15}$$

where $\alpha(t)$ is the effective Regge trajectory. Using the fits from Table V, together with the 10.4-GeV results,[33] both evaluated at $t = -0.4$ GeV^2, yields $\alpha(-0.4) = 0.27 \pm 0.07$. This can be compared with the value $\alpha(-0.4) = 0.14$ found[35] for $\pi^- p \to \pi^0 n$, for which only $C = -1$ exchange is allowed in the t channel.

The shape of $\Delta(t)$ resembles that of the Bessel function $J_0(R_-\sqrt{-t})$, suggesting that $C = -1$ amplitude is strongly absorbed with most of the contribution coming from the periphery of the interaction region.[34] Equating the crossover point with the first zero of the Bessel function $J_0(R_-\sqrt{-t})$ gives a typical interaction radius for the source of the $C = -1$ amplitude in impact-parameter space,

$$R_- = 0.475/\sqrt{-t_c}\ \text{F}, \tag{16}$$

for t_c in GeV^2. This is compared in Table XII with a typical radius for the $C = +1$ amplitude derived from the forward logarithmic slope B of the quantity

$$\Sigma = \frac{1}{2}\left[\frac{d\sigma}{dt}(x^- p) + \frac{d\sigma}{dt}(x^+ p)\right]. \tag{17}$$

Using the black disk approximation, $B = R_+^2/4$, or for B in GeV^{-2},

$$R_+ = 0.395\sqrt{B}\ \text{F}. \tag{18}$$

With these definitions $R_-/R_+ = 1$ to within about 10% for both Kp and pp from 4 to 100 GeV.

TABLE IX. Single-Regge-pole fit to elastic data: $d\sigma/dt = A_{s_0} \exp(B_{s_0} t + C_{s_0} t^2)(s/s_0)^{2(\alpha_0 + \alpha' |t|) - 2}$.

	A_{s_0} (mb/GeV^2)	B_{s_0} (GeV^{-2})	C_{s_0} (GeV^{-4})	α_0	α' (GeV^{-2})	χ^2/degf
$\pi^+ p$	28.09 ± 0.24	8.89 ± 0.07	2.12 ± 0.11	1.013 ± 0.005	−0.057 ± 0.021	$\frac{93}{81}$
$K^+ p$	18.29 ± 0.30	8.20 ± 0.14	2.09 ± 0.24	1.059 ± 0.012	−0.147 ± 0.053	$\frac{65}{69}$
pp	74.88 ± 0.69	10.77 ± 0.08	1.88 ± 0.14	0.981 ± 0.006	−0.203 ± 0.025	$\frac{95}{76}$
$\pi^- p$	29.58 ± 0.23	9.39 ± 0.06	2.66 ± 0.10	0.990 ± 0.005	−0.036 ± 0.020	$\frac{157}{78}$
$K^- p$	21.13 ± 0.49	8.94 ± 0.23	2.48 ± 0.41	1.012 ± 0.017	−0.059 ± 0.079	$\frac{66}{61}$
$\bar{p}p$	86.18 ± 1.75	12.34 ± 0.22	2.96 ± 0.50	0.924 ± 0.015	0.167 ± 0.091	$\frac{95}{62}$

TABLE X. Slope of effective Regge trajectory at $-t = 0.2$ GeV^2. [1% systematic uncertainty added in quadrature to errors on $B(-0.2)$. This corresponds to the *energy-dependent* part of the total systematic uncertainty of $1\frac{1}{2}$%.]

Reaction	$\alpha'(-0.2)$ (GeV^{-2})
pp	-0.27 ± 0.06
$\bar{p}p$	$+0.10 \pm 0.09$
K^+p	-0.18 ± 0.06
K^-p	-0.07 ± 0.07
π^+p	-0.09 ± 0.05
π^-p	-0.02 ± 0.05

E. Total elastic cross section

The energy dependence of the total elastic cross section, σ_{el}, is shown for the six reactions in Fig. 23. In all cases, σ_{el} falls away rapidly in energy (consistent with power-law behavior) but then levels off at high energy and becomes nearly constant. The rapid fall at low energy is consistent with the crude Regge-pole estimate $\sigma_{el} \sim s^{-2\alpha'|\langle t \rangle|}$, where $\langle t \rangle$ is the average value of t.[36] The leveling off is associated with the fact that both the "Pomeron" slope α' and $\langle t \rangle$ are decreasing. The declining contribution of the elastic channel to the total cross section contrasts with the rising value of the total inelastic cross section for all particles except $\bar{p}$. The cancellation of these two effects in the low-energy region is responsible for the apparently flat behavior of the total cross section. Once the total elastic contribution stops declining the increase in the total cross section due to inelastic contributions becomes manifest.

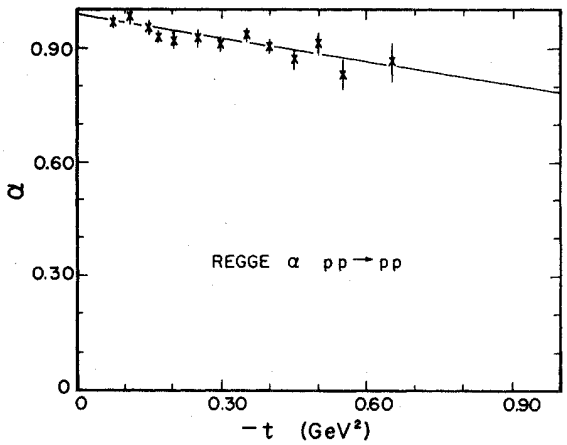

FIG. 18. Regge α parameter determined from the proton-proton elastic scattering results of this experiment. The straight line is the best fit to the data, as given in Eq. (9).

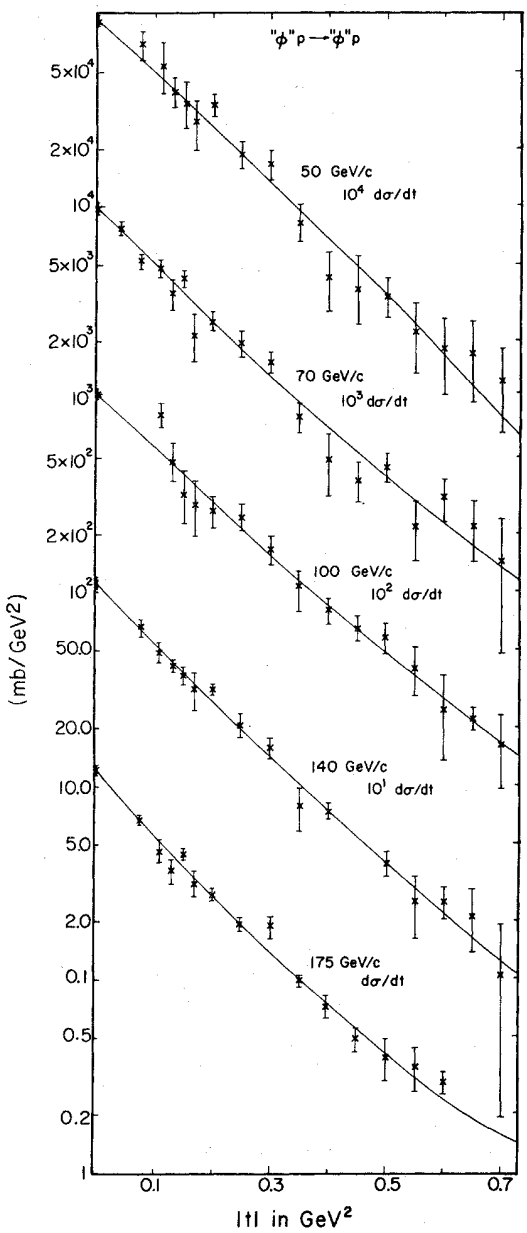

FIG. 19. "ϕ"p elastic cross section calculated from Eq. (12) using cross-section values of Table IV. The results for 50, 70, 100, 140, and 175 GeV/c are scaled by 10 000, 1000, 100, 10, and 1, respectively, to provide separation between the curves. The values at $t = 0$ are calculated from the optical points for pion and kaon scattering according to Eq. (11).

F. Geometric scaling

The hypothesis of geometric scaling (GS) was introduced[37,38] to correlate various results from pp elastic-scattering and total-cross-section measurements at ISR energies. It may be stated in terms of the elastic scattering amplitude

TABLE XI. Quadratic-exponential fits to $d\sigma(\phi p)/dt$: Fits of the differential elastic scattering cross section for ϕp as defined in (12) to the form $d\sigma/dt = Ae^{B|t|+Ct^2}$. The optical-theorem prediction (OTP) as calculated from (11) is included as a data point with a 3% uncertainty.

p (GeV/c)	OTP (mb/GeV^2)	A (mb/GeV^2)	B (GeV^{-2})	C (GeV^{-4})	$B(-0.2)$ (GeV^{-2})	$P(\chi^2)$	degf
50	9.26	9.31±0.23	−6.06±0.51	−1.02±1.16	−6.47±0.18	0.78	14
70	9.91	9.89±0.30	−7.19±0.52	1.55±1.12	−6.57±0.19	0.27	15
100	10.92	10.95±0.28	−6.66±0.44	1.08±0.81	−6.22±0.16	0.72	13
140	11.62	11.57±0.28	−7.34±0.32	1.41±0.70	−6.78±0.12	0.81	14
175	12.29	12.19±0.33	−7.92±0.32	2.47±0.69	−6.94±0.13	0.56	14

$$A(s,b) = \frac{(e^{2i\delta(b)} - 1)}{i},$$

in impact-parameter space [where $\delta(b)$ is the elastic phase shift]:

$$A(s,b) = A(b/R(s)), \tag{19}$$

where $R(s)$ is a range parameter containing all the energy dependence. From this property, it follows that the total cross section, σ_{tot}, the total elastic cross section, σ_{el}, and the forward elastic slope parameter, B, all depend on energy in the same way. Specifically σ_{el}/σ_{tot} and B/σ_{tot} are independent of energy. Furthermore, the quantity $1/\sigma_{tot}{}^2 d\sigma/dt$ plotted against $\sigma_{tot}\ t$ is predicted to be independent of energy.

Table VII lists the ratio of σ_{el}/σ_{tot} for the reactions measured in this experiment. Figure 24 shows these results plotted together with results from other experiments above a few GeV. Two important observations are (i) all hadrons are not alike. σ_{el}/σ_{tot} is ~0.18 for pp and $\bar{p}p$ scattering but is only ~0.13 for kaons and pions; (ii) each of the six elastic channels reaches a constant value of σ_{el}/σ_{tot} by 100 GeV. Especially impressive is the fact that the value 0.18 for pp scattering is observed from 100 GeV to ISR energies (equivalent to a lab energy of 1480 GeV).

The most convincing test of GS within this experiment comes in K^+p scattering where the total cross section is already increasing (by ~6%) across this energy range. Figure 25 presents a "differential" test of GS. The smooth curves are calculated from the fits to the 70-GeV/c results. The points are the 175-GeV/c cross-section values scaled by the ratio $[\sigma_{tot}(70)/\sigma_{tot}(175)]^2$ and plotted against the scaled t value, $t\sigma_{tot}(175)/\sigma_{tot}(70)$. The 175- and 70-GeV/$c$ total cross sections are in the ratio of 1.06 for K^+p and 1.01 for pp. Because the

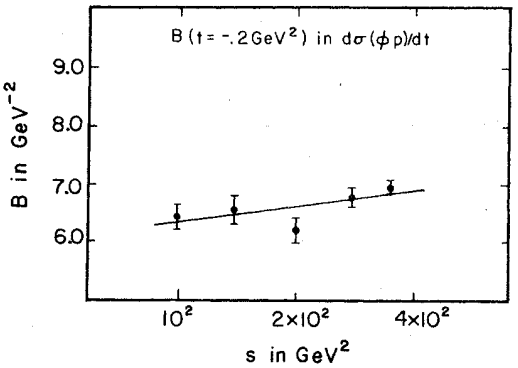

FIG. 20. s dependence of slope parameter for "ϕ"p elastic scattering at $-t = 0.2$ GeV^2. The smooth curve has a slope of 0.2 GeV^{-2}, the value observed in pp scattering.

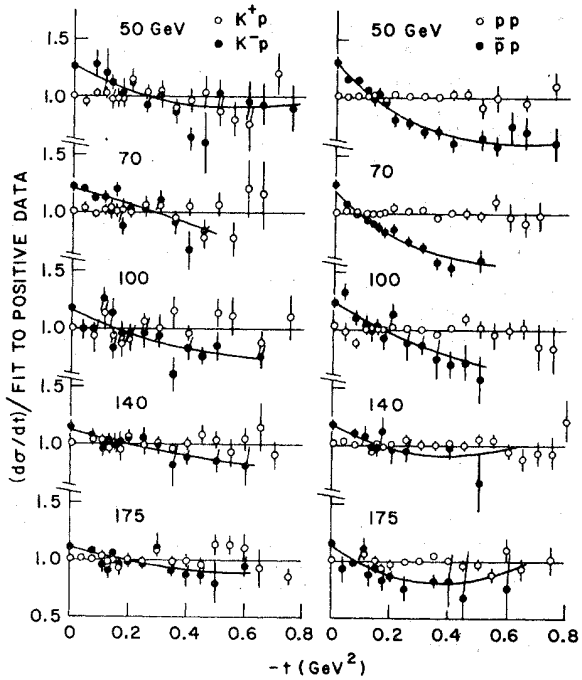

FIG. 21. Elastic scattering cross sections divided by the quadratic exponential fits of Table V to the positive-beam data. The line shows the ratio of negative-beam fits to positive-beam fits.

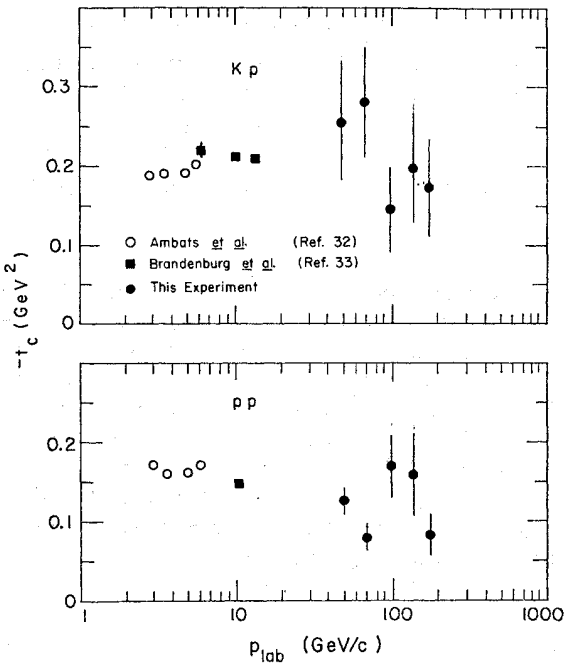

FIG. 22. Crossover points as a function of incident momentum.

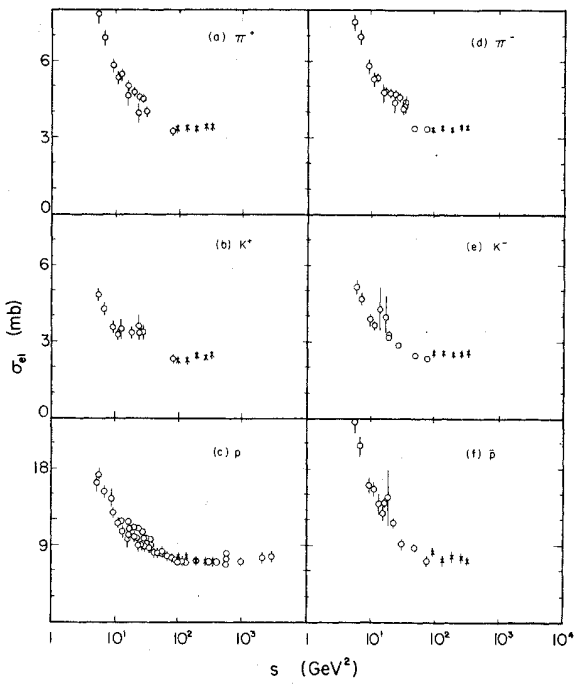

FIG. 23. Total elastic cross sections for all six particles vs s. The crosses are from Table VII.

total cross sections change so little, the scaling does not have a great effect. Nevertheless, the scaling seems to work reasonably well for K^+p but fails for pp. This is consistent with the observations based on the ratio σ_{el}/σ_{tot} that GS is not satisfied for pp below 100 GeV/c.

Figure 26 compares the results for protons at 175 GeV/c with ISR results[39] at lab equivalent energies of 290 and 1480 GeV. The ISR results are scaled to 175 GeV/c. The two ISR results scale between themselves quite well. The scaling with the 175-GeV/c results of this experiment is good to ~5% at low t and ~15% at $-t>0.2$ GeV^2. The departures from scaling are not significant in view of the large normalization uncertainties on the ISR data.

TABLE XII. Typical radii R_+ and R_- in impact-parameter space for $C=+1$ and $C=-1$ exchange amplitudes, as defined above. The uncertainties in $R_\pm$ are typically ±2% except for R_- at 100 GeV/c (±10%).

	P (GeV/c)	R_+ (F)	R_- (F)	R_-/R_+
Kp	4	1.00	1.09	1.09
	100	1.15	1.09	0.95
pp	4	1.33	1.18	0.89
	100	1.33	1.43	1.08

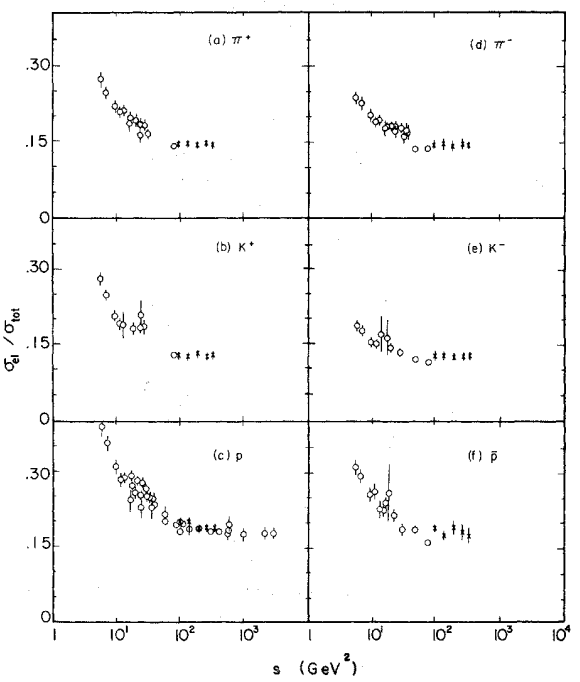

FIG. 24. Ratio of σ_{el}/σ_{tot} vs s. The circles represent values taken from Ref. 28. The crosses are from Table VII.

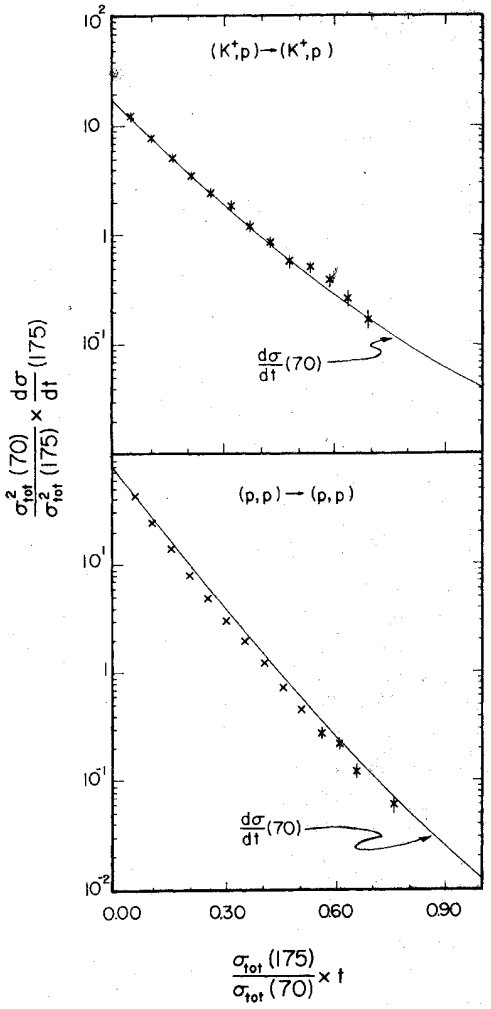

FIG. 25. Geometric-scaling test for K^+p and pp differential cross sections between 70 and 175 GeV/c.

The results of this experiment suggest, but do not prove, that GS is a general property of hadron elastic scattering at high energies. Since only a limited range of energies is covered, it is still possible that GS predictions are satisfied "accidentally" and will fail at even higher energies. To establish conclusively this scaling law, it will be necessary to make measurements at even higher energies where the total cross section has already increased significantly. Precise measurement of $K^{\pm}p$ scattering at the highest energies available in secondary beams at Fermilab would be especially important.

If GS is confirmed, it will provide an important guideline for model development. For example, conventional Regge models with poles do not exhibit GS behavior.

G. Impact-parameter representation

The differential elastic scattering cross sections given in Table IV have been numerically transformed into impact-parameter space[40]:

$$\mathrm{Im}h_{\mathrm{el}}(s,b)=\frac{1}{\sqrt{4\pi}}\int_0^{\sqrt{0.75}}\left(\frac{d\sigma}{dt}\right)^{1/2}J_0(b\sqrt{-t})\sqrt{-t}\,d(\sqrt{-t}) \tag{20}$$

and corrected for large-t contributions. The error in this correction is 2% for small impact-parameter values and negligible for $b>0.2$ F. The error due to the contribution of the real part of the elastic scattering amplitude is not very model dependent and can be shown to be ~3%.[40] Under the assumption that the elastic scattering amplitude is mainly imaginary, then its Bessel transform, $\mathrm{Im}h_{\mathrm{el}}(s,b)$, satisfies in impact-parameter space a unitarity equation of the form

$$\begin{aligned}\mathrm{Im}h_{\mathrm{el}}(s,b)&=\tfrac{1}{4}|h_{\mathrm{el}}(s,b)|^2+G_{\mathrm{inel}}(s,b)\\&\approx\tfrac{1}{4}|\,\mathrm{Im}h_{\mathrm{el}}(s,b)|^2+G_{\mathrm{inel}}(s,b)\,,\end{aligned} \tag{21}$$

where $G_{\mathrm{inel}}(s,b)$ is defined by its relation to σ_{inel} as follows:

$$\sigma_{\mathrm{inel}}=\pi\int G_{\mathrm{inel}}(s,b)\,db^2\,.$$

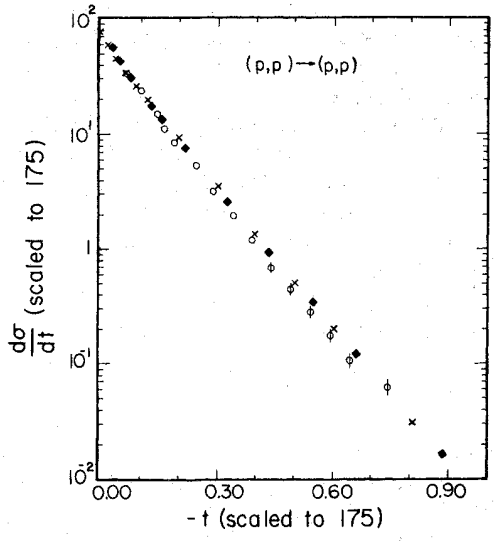

FIG. 26. Geometric-scaling test for pp differential cross sections between 175 GeV/c and 290 and 1480 GeV/c equivalent energy from ISR (Ref. 39). Open circles are the 175-GeV/c results of this experiment. Crosses and diamonds are the 290- and 1480-GeV/c results scaled as follows: t values are multiplied by $\sigma_{\mathrm{tot}}(290)/\sigma_{\mathrm{tot}}(175)$ and $\sigma_{\mathrm{tot}}(1480)/\sigma_{\mathrm{tot}}(175)$, respectively; cross sections are multiplied by $\sigma_{\mathrm{tot}}{}^2(175)/\sigma_{\mathrm{tot}}{}^2(290)$ and $\sigma_{\mathrm{tot}}{}^2(175)/\sigma_{\mathrm{tot}}{}^2(1480)$, respectively.

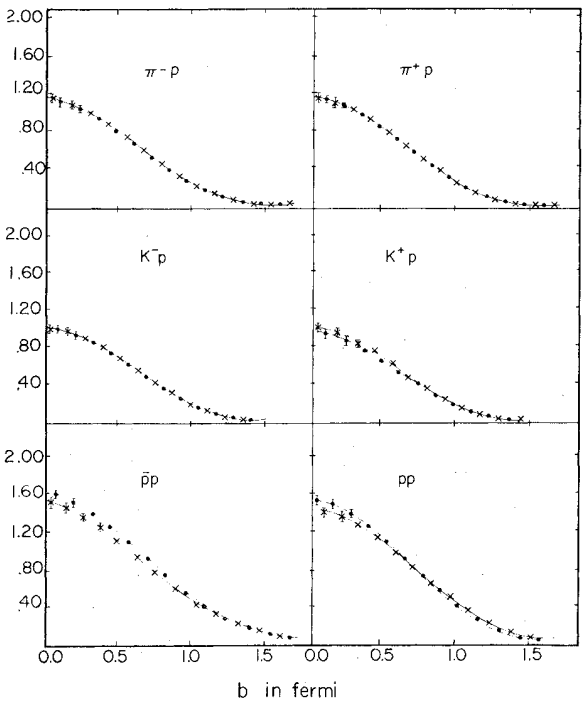

FIG. 27. $\mathrm{Im}h_{\mathrm{el}}(s,b)$ for the six reactions at 50 GeV/c (circles) and at 175 GeV/c (crosses). The errors shown include the statistical errors, the uncertainty due to the real part and to large-t contributions ($0.75 \leq |t| \leq 1.4$ GeV^2).

The left-hand side can be identified with the total cross section in b space ($d^2\sigma_t/\pi db^2$) and the right-hand side is the sum of the elastic ($d^2\sigma_{\mathrm{el}}/\pi db^2$) and inelastic ($d\sigma_{\mathrm{inel}}/\pi db^2$) cross sections. Therefore the knowledge of $\mathrm{Im}h_{\mathrm{el}}(s,b)$ permits the calculation of the total and inelastic cross sections in impact-parameter space.

Figure 27 shows the $\mathrm{Im}h_{\mathrm{el}}(s,b)$ distribution for the six reactions at incoming momenta of 50 and 175 GeV/c. Figure 28 shows a plot of $\mathrm{Im}h_{\mathrm{el}}(s,b=0)$ as a function of p_{lab} for all the reactions discussed in this paper. It can be seen that all the reactions are consistent with having very little change as a function of energy except for $p^{\pm}p$. However, a straightforward implication of geometric scaling is

$$\mathrm{Im}h_{\mathrm{el}}(s,b=0) = \mathrm{const} \tag{22}$$

for all s. Therefore the previous statement that pp is inconsistent with geometric scaling for $p_{\mathrm{lab}} < 100$ GeV also follows from the decrease of $\mathrm{Im}h_{\mathrm{el}}(s,b=0)$, while for $s > 200$ GeV^2, it stays constant (even through the ISR region). Figure 29 is a plot of $G_{\mathrm{inel}}(s,b=0)$ as a function of s, that is, the absorption probability for a head-on collision. For a comparison, also shown are the results of a similar calculation done for pp with ISR data and a $p_{\mathrm{lab}} = 24$-GeV/c experiment.[41] Thus a baryon has a ~6% probability of colliding head-on with a proton without any absorption, while this probability is ~18% for pions and ~25% for kaons. As one can see, mesons, as seen by protons, are very transparent objects.

Figure 30 shows the rms interaction distance for the total and inelastic cross sections, defined by

$$R_i = \left[\int_0^{b_{\max}} b^2 (d^2\sigma_i/db^2)\, b\,db \Big/ \int_0^{b_{\max}} (d^2\sigma_i/db^2)\, b\,db \right]^{1/2}, \tag{23}$$

where i = total or inelastic, and $b_{\max} = 1.6$ F. With the exception of K^-p and $\bar{p}p$, R_i is consistent with being an increasing function of s for $s > 140$ GeV^2.

It has been shown above that even in this energy range the differential elastic cross sections of $K^{\pm}p$ and $p^{\pm}p$ show the crossover phenomenon, which is assumed to be due to the interference between nonflip ω exchange and Pomeron exchange. The ω-exchange contribution to K^-p and $\bar{p}p$ can be seen in impact-parameter space[42] by looking at the distribution

$$\Delta^{xp}(s,b) \equiv \mathrm{Im}h_{\mathrm{el}}^{x^-p}(s,b) - \mathrm{Im}h_{\mathrm{el}}^{x^+p}(s,b), \tag{24}$$

where $x = K, p$. Those distributions are shown in Fig. 31 for Kp and pp, respectively, at $p_{\mathrm{lab}} = 50$ GeV/c and $p_{\mathrm{lab}} = 175$ GeV/c. It can be seen that those distributions are peripheral and that the ω-exchange contribution decreases very fast with energy, in particular, in $\bar{p}p$ (this is expected from the energy dependence of regular Regge trajectories).

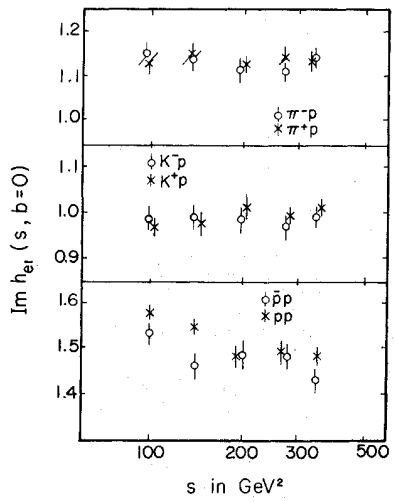

FIG. 28. $\mathrm{Im}h_{\mathrm{el}}(s,b=0)$ as a function of s for $\pi^{\pm}p$, $K^{\pm}p$, and $p^{\pm}p$. The errors are calculated as for Fig. 27.

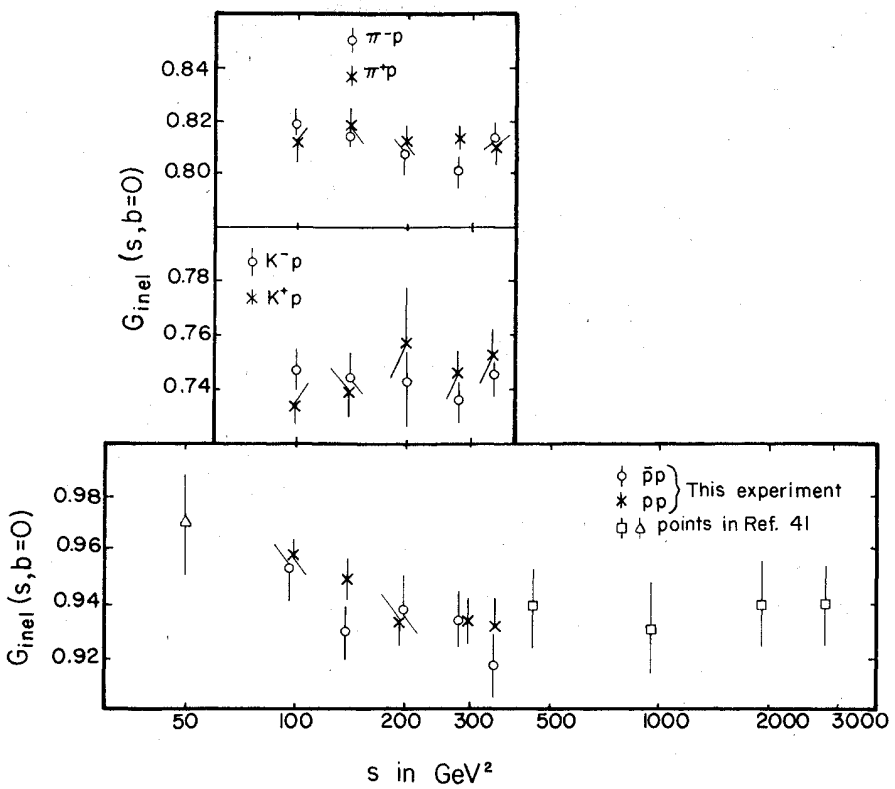

FIG. 29. $G_{\text{inel}}(s, b=0)$ as a function of s for $\pi^{\pm}p$, $K^{\pm}p$, and $p^{\pm}p$. The errors are calculated as for Fig. 27. The ISR and 24-GeV/c points in pp are taken from Ref. 41.

H. Ratio of total elastic of total cross section

The six elastic scattering reactions are characterized by different values of $R=\sigma_{\text{el}}/\sigma_{\text{tot}}$. In particular, the distinction between meson-nucleon channels with $R=0.13$ to 0.14 and nucleon-nucleon ($pp, \bar{p}p$) channels with $R\sim 0.18$ is observed. The pp values are very close to the so-called Van Hove ratio[17]:

$$R_{\text{VH}}=1-(4-4\ln 2)^{-1}=0.185. \tag{25}$$

This ratio emerges from a model in which elastic scattering is obtained as the shadow scattering of inelastic reactions, crudely described by a very simple model. The model amounts to assuming a Gaussian inelastic overlap function $G_{\text{inel}}(s,b)$ with a value of unity at $b=0$. From the impact-parameter inversion of the elastic cross sections, these conditions were seen to be approximately satisfied by pp and $\bar{p}p$, but the meson-nucleon interactions had $G_{\text{inel}}(s,0)$ much less than 1. For all the channels, R is much less than $\frac{1}{2}$—the black-disk limit.

I. Quark-model predictions

Simple quark counting would imply the following relations for the elastic amplitudes S [under the assumption that the exchanged particle is an SU(3) singlet]:

$$S(\pi p)=S(Kp), \tag{26a}$$

$$S(Kp)=\tfrac{2}{3}S(pp). \tag{26b}$$

Relations (26a) and (26b) are plotted in Fig. 32 for $p_{\text{lab}}=50$ GeV/c and $p_{\text{lab}}=175$ GeV/c, where $S(xp)$ is defined by[43]

$$2S(x,p)=[d\sigma(x^+p)/dt+d\sigma(x^-p)/dt]^{1/2} \tag{27}$$

for $x=\pi, K, p$. Relation (26b) is clearly not satisfied in all the t range; however, (26a) is consistent with being satisfied for $|t|\gtrsim 0.4$ GeV^2 but it is badly violated at small t values. This is consistent with the Chew-Rosenzweig[44] model that claims that the Pomeron and the f are the same Reggeon and the SU(3) structure of this pole and its mixing with the f' pole change as a function of t to make the Kp and πp amplitudes equal at high t.

Lipkin[45] has suggested that the Pomeron has two components, one that satisfies relations (26a) and (26b) and a second component satisfying

$$S(\pi p)=2S(Kp)=\tfrac{4}{9}S(pp). \tag{28}$$

Combining the two components, the following re-

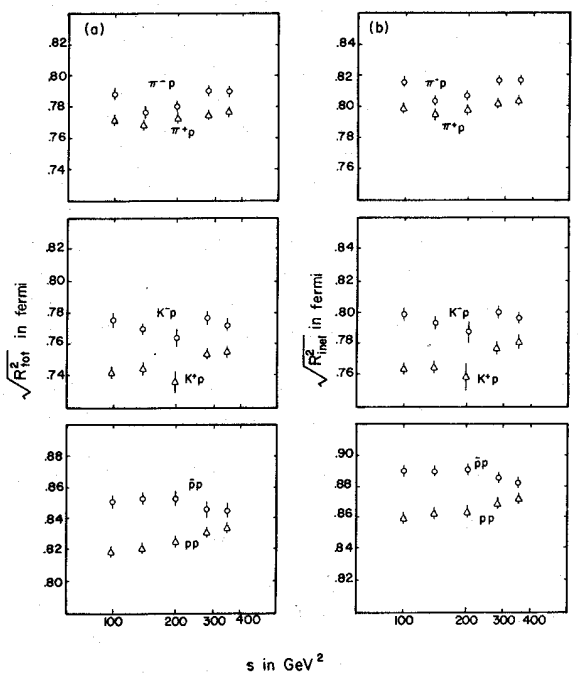

FIG. 30. The rms interaction distances for (a) the total and (b) the inelastic cross sections as a function of s for all six reactions. The errors are calculated as for Fig. 27. These values are appropriate for comparing the different reactions even though they may all increase by as much as 12% if the integration region is extended to $b = 2$ F.

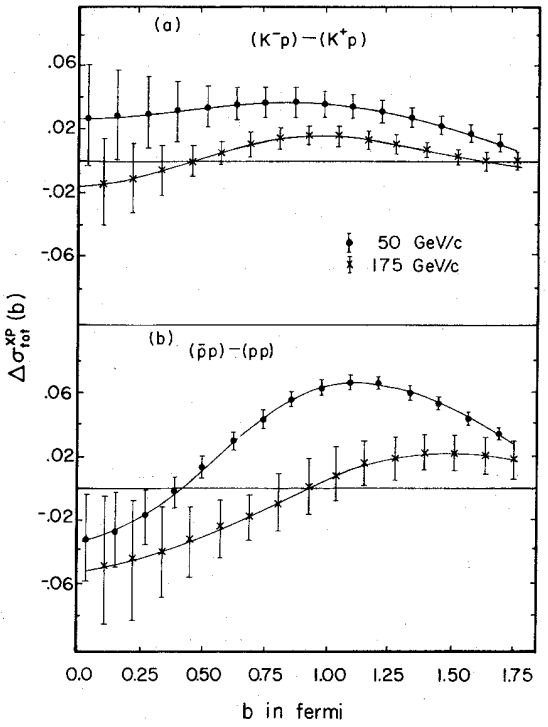

FIG. 31. $\Delta\sigma^{xp}_{tot}(b)$ for (a) Kp and (b) pp at $p = 50$ GeV/c (circles) and at $p = 175$ GeV/c (crosses).

lation should be satisfied

$$S(\pi p) = \tfrac{1}{2}S(Kp) + \tfrac{1}{2}S(pp)\,. \tag{29}$$

This relation is very well satisfied for the optical points ($t = 0$); however, as we can see in Fig. 32, it becomes worse the higher the t value.

IX. CONCLUSION

The small- and intermediate-t elastic scattering of $\pi^\pm$, $K^\pm$, p, and $\bar{p}$ on protons has been measured in the (50 to 175)-GeV energy range. While the concept of diffraction scattering provides a convenient framework for understanding the results, the idea that the cross sections for all reactions would be clearly dominated by the Pomeron pole is apparently not realized even at these high energies. The similar shrinkage pattern of the K^+p and pp diffraction peaks encourages the belief that the Pomeron does rule these channels, but the energy independence of $\pi^\pm p$ and K^-p, together with the slow antishrinkage of $\bar{p}p$, indicates that the lower-lying neutral-meson trajectories are still important. The crossover phenomenon between particle and antiparticle elastic scattering continues to be observed. The position of the kaon crossover is

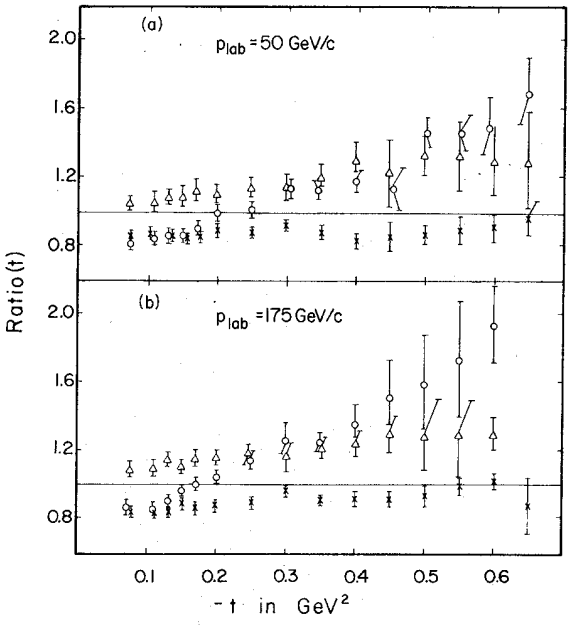

FIG. 32. Quark-model ratios at (a) $p = 50$ GeV/c and (b) $p = 175$ GeV/c. The different ratios are (circles) $\frac{3}{2}S(Kp)/S(pp)$ (crosses) $S(Kp)/S(\pi p)$, and (triangles) $S(\pi p)/[\frac{1}{2}S(Kp) + \frac{1}{3}S(pp)]$.

relatively energy independent from a few GeV/c to 175 GeV/c, but the nucleon crossover may be moving toward smaller t. The predictions of the geometric-scaling hypothesis seem to be satisfied by $\pi^{\pm}p$ and $K^{\pm}p$ across the whole energy range but by pp only above 100 GeV/c. The impact-parameter representation demonstrates the differences between nucleon-nucleon (pp or $\bar{p}p$) scattering and meson-nucleon scattering. The protons seem to be very opaque with respect to nucleon projectiles but surprisingly transparent to mesons. The contribution of the odd C-parity meson trajectories is shown to be peripheral in b space.

ACKNOWLEDGMENTS

We would like to express our thanks to the many people at the Fermi National Accelerator Laboratory who have contributed to the successful operation of the Single Arm Spectrometer and of the accelerator. We would like to thank the Meson Laboratory staff and, in particular, John Satti, the $M6$-SAS engineer, and Stan Ecklund, the $M6$ liaison physicist. Karl Brown and David Carey made major contributions to the optical design of the beam and spectrometer. This experiment would not have been possible without the combined efforts of the members of the support groups of the participating institutions. We would like to thank in particular: Len Filips and Gene Walschon from Argonne National Laboratory, Brian Heltsley and David Rossi from Brown University, Travis Minto from Fermilab, Arcangelo Distante, Michele Perchiazzi and Angelo Sachetti from Instituto Nazionale di Fisica Nucleare, Bari, Italy, Tommy Lyons from MIT, Michael Jordan from Northeastern University, and John Grant, Jack Schroeder and Justin Escalero from SLAC.

*Work supported in part by the U. S. Energy Research and Development Administration under Contract No. E(11-1)-3069 (MIT LNS), and Contract No. E(11-1)-3130B (Brown), by the National Science Foundation under Contract No. LNS-NSF-GP-29543 (LNS Cornell), and by the Instituto Nazionale di Fisica Nucleare (Italy). Experiment conducted at the Fermi National Accelerator Laboratory, Batavia, Illinois.

†Current address: Daresbury Nuclear Physics Laboratory, Daresbury, Lancashire, England.

‡Also at Centre d'Etudes Nucléaires de Saclay, 91 Gir-sur-Yvette, France.

§Current address: University of Chicago, Chicago, Illinois 60637.

‖Current address: University of Utah, Salt Lake City, Utah 84112.

¶Current address: University of Illinois, Urbana, Illinois 61801.

**Also at Centre d'Etudes Nucléaires de Saclay, 91 Gif-sur-Yvette, France.

[1]Fermilab Single Arm Spectrometer Group, Phys. Rev. Lett. 35, 1195 (1975).

[2]R. L. Anderson *et al.*, Phys. Rev. Lett. 37, 1025 (1976).

[3]R. Anderson *et al.*, Phys. Rev. Lett. 37, 1111 (1976).

[4]R. Anderson and J. Grant, Nucl. Instrum. Methods 135, 267 (1976).

[5]M. Benot, J. Litt, and R. Meunier, Nucl. Instrum. Methods 105, 431 (1972).

[6]D. Ayres, ANL report, 1974 (unpublished).

[7]M. Sogard and A. Weitsch, Fermilab Report No. TM-517, 1974 (unpublished).

[8]K. L. Brown, SLAC Report No. 75 (unpublished); K. L. Brown and S. K. Howry, SLAC Report No. 91 (unpublished).

[9]J. T. Massimo, B. Nelson, and L. J. Levinson, Brown University High Energy Group Internal Reports Nos. 123, 124, and 125, 1972 (unpublished); L. J. Levinson *et al.*, Bull. Am. Phys. Soc. 20, 593 (1975).

[10]B. Gottschalk, SLAC Report No. TN-74-15, 1974 (unpublished).

[11]J. Butler, M.I.T. Ph.D. thesis, 1975 (unpublished).

[12]S. P. Denisov *et al.*, Nucl. Phys. B61, 62 (1973).

[13]H. A. Bethe, Ann. Phys. (N.Y.) 3, 190 (1958); K. J. Foley *et al.*, Phys. Rev. 181, 1775 (1969).

[14]G. B. West and D. R. Yennie, Phys. Rev. 172, 1413 (1968).

[15]A. S. Carroll *et al.*, Phys. Rev. Lett. 33, 928 (1974); 33, 932 (1974).

[16]M. R. Sogard, Phys. Rev. D 9, 1486 (1974).

[17]L. Van Hove, Rev. Mod. Phys. 36, 655 (1964).

[18]V. Bartenev *et al.*, Phys. Rev. Lett. 31, 1369 (1973).

[19]D. P. Sidhu and U. P. Sukhatme, Phys. Rev. D 11, 135 (1975); R. E. Hendrick and B. Lautrup, *ibid.* 11, 529 (1975).

[20]J. Lach, Report No. Fermilab/Conf./75/15/Exp, invited talk at the Triangle Conference on High Energy Particle Interactions, Bratislava, Czechoslovakia, 1975 (unpublished).

[21]Yu. M. Antipov *et al.*, Nucl. Phys. B57, 333 (1973).

[22]A. Derevchekov *et al.*, Phys. Lett. 48B, 367 (1974).

[23]V. Bartenev *et al.*, Phys. Rev. Lett. 31, 1088 (1973).

[24]C. W. Akerlof *et al.*, Phys. Rev. Lett. 35, 1406 (1975); D. Yovanovitch (private communication).

[25]G. Barbiellini *et al.*, Phys. Lett. 39B, 663 (1972).

[26]R. A. Carrigan, Jr., Phys. Rev. Lett. 24, 168 (1970).

[27]R. K. Carnegie *et al.*, Phys. Lett. 59B, 313 (1975).

[28]M. Aderholz *et al.*, Phys. Lett. 24B, 434 (1967). C. W. Akerlof *et al.*, Phys. Rev. Lett. 35, 1406 (1975); U. Amaldi *et al.*, Phys. Lett. 36B, 504 (1971); U. Amaldi *et al.*, *ibid.* 43B, 231 (1973); I. Ambats *et al.*, Phys. Rev. D 9, 1179 (1974); Yu. M. Antipov *et al.*, Ref. 21; V. Bartenev *et al.*, Phys. Rev. Lett. 29, 1755 (1972); J. Bartsch *et al.*, Nucl. Phys. B29, 398 (1971); D. Birnbaum *et al.*, Phys. Rev. Lett. 23, 663 (1969); S. Brandt *et al.*, *ibid.* 10, 413 (1963); C. Bromberg *et al.*, *ibid.* 31, 1563 (1973); Kh. M. Chernev *et al.*, Phys. Lett. 36B, 266 (1971); A. A. Derevchekov *et al.*, *ibid.* 48B, 367 (1974); A. N. Diddens *et al.*, Phys. Rev. Lett. 9, 108 (1962); A. N. Diddens *et al.*, *ibid.* 9, 111 (1962); A. R. Dzierba *et al.*, Phys. Rev. D 7, 725 (1973); R. M. Edelstein *et al.*, *ibid.* 5, 1073 (1972); A. Firestone *et al.*, *ibid.* 10, 2080 (1974); K. J. Foley

et al., Phys. Rev. Lett. 11, 425 (1963); K. J. Foley *et al.*, *ibid.* 11, 503 (1963); K. J. Foley *et al.*, *ibid.* 15, 45 (1965); D. Fong *et al.*, Phys. Lett. 53B, 290 (1974); D. Harting *et al.*, Nuovo Cimento 38, 60 (1965); P. L. Jain *et al.*, Nucl. Phys. B19, 568 (1970); R. J. Miller *et al.*, Phys. Lett. 34B, 230 (1971).

[29]K. J. Foley *et al.*, Phys. Rev. Lett. 15, 45 (1965).

[30]C. Quigg and E. Rabinovici, Phys. Rev. D 13, 2525 (1976).

[31]V. Barger, K. Geer, and F. Halzen, Nucl. Phys. B44, 475 (1975).

[32]I. Ambats *et al.*, Phys. Rev. D 9, 1179 (1974).

[33]G. Brandenburg *et al.*, Phys. Lett. 58B, 367 (1975); 58B, 371 (1975).

[34]M. Davier and H. Harari, Phys. Lett. 40B, 281 (1972).

[35]A. V. Barnes *et al.*, Phys. Rev. Lett. 37, 76 (1976).

[36]V. Barger and D. Cline, *Phenomenological Theories of High Energy Scattering* (Benjamin, New York, 1969), p. 66.

[37]J. Dias de Deus, Nucl. Phys. B59, 231 (1973).

[38]A. J. Buras and J. Dias de Deus, Nucl. Phys. B71, 481 (1974).

[39]P. Kroll (private communication).

[40]D. S. Ayres *et al.*, Phys. Rev. D 14, 3092 (1976).

[41]H. I. Miettinen, in *High Energy Hadronic Interactions*, proceedings of the IX Rencontre de Moriond, 1974, edited by J. Tran Thanh Van (CNRS, Paris, 1974).

[42]M. Davier and H. Harari, Phys. Lett. B40, 281 (1972).

[43]H. Lipkin (private communication).

[44]C. Rosenzweig and G. F. Chew, Phys. Lett. 58B, 93 (1975).

[45]H. J. Lipkin, Phys. Lett. B56, 76 (1975).